Characterization of Metal Aerosol in Micro Metal Dust Burner (M2DB)

Shanmugam, Ranjith Kumar

Award date:
2018

Technische Universiteit
Eindhoven
University of Technology

Department of Mechanical Engineering
Multiphase & Reactive Flows

Characterization of Metal Aerosol in Micro Metal Dust Burner (M^2DB)

Master Thesis

For obtaining the degree of
Master of Science in Automotive Technology at the
department of Mechanical Engineering of Eindhoven
University of Technology.

Ranjith Kumar Shanmugam - 0980721
r.k.shanmugam@student.tue.nl

Graduation Committee:

Prof. Dr. L.P.H. De Goey	Eindhoven University of Technology	Chair /Supervisor
Dr. Y.L. Shoshin	Eindhoven University of Technology	Supervisor
Dr. N.J. Dam	Eindhoven University of Technology	Supervisor
Dr. J.P. Hofmann	Eindhoven University of Technology	

Eindhoven, Friday 24th August, 2018

Technische Universiteit
Eindhoven
University of Technology

Declaration concerning the TU/e Code of Scientific Conduct for the Master's thesis

I have read the TU/e Code of Scientific Conduct[i].

I hereby declare that my Master's thesis has been carried out in accordance with the rules of the TU/e Code of Scientific Conduct

Date

24-08-2018

Name

RANJITH KUMAR SHANMUGAM

ID-number

0980721

Signature

S. Ranjith Kumar

Submit the signed declaration to the student administration of your department.

[i] See: http://www.tue.nl/en/university/about-the-university/integrity/scientific-integrity/
The Netherlands Code of Conduct for Academic Practice of the VSNU can be found here also.
More information about scientific integrity is published on the websites of TU/e and VSNU

Abstract

This thesis focuses on the detailed study of metal aerosol lifted flames properties such as particle velocity and particle density. A small metal dust burner is used to produce a small and stable aerosol flame. In order to study the high purity carbonyl iron particle in the flame at different initial temperatures, the central jet and the shroud flow are preheated. An optical setup is used to analyze the velocity of the particle, and number density is estimated by captured combustion products. Moreover, the burner is optimised for efficient consumption of metal powder inside the dispersion chamber. The heating system to preheat the gas flow is discussed, and the temperature profile based on different radius and height of the gas flow are determined. Furthermore, the captured iron oxides during number density estimation are analysed in optical and scanning electron microscopes to find the diameter of the products formed. Finally, an investigation of zinc aerosol combustability with different oxygen concentration and temperature is carried out.

Preface

This master thesis marks the end of my masters degree in Automotive Technology at the Eindhoven University of Technology. Many people have contributed in a variety of ways to make this thesis successful. Without the help of them, it was impossible to finish this project.

At first, I want to thank my graduation supervisor Prof.dr. L.P.H. (Philip) de Goey, who gave this opportunity to work in this new field of study related to metal fuels.

My heartiest thanks to Dr. Y.L. Shoshin and Dr. N.J. Dam, who were my thesis supervisors during my master thesis. They supported and motivated throughout my thesis by giving his knowledge and support. Without their guidance, I could not complete this Master thesis and as well as my degree. From the start to the end of this thesis, their constant advice, thoughts helps me to think in various angles in this project. With their guidance, I have learned a lot of things during this project.

During the experiments whenever i faced issues, I experienced great support from the staff. For this I would especially like to thank Martjin and Theo who helped me during this project at various stages. I would also like to thank all my friends in Eindhoven who gave me good memories during this study period.

Finally, I would like to thank my father Shanmugam, my mother Malarkodi, my sister Kirthika and my girl friend Keerthana shree for their unconditional love and support at all my stages of my life. Without my parents, I would never have enjoyed so many opportunities in my life.

Once again, Thank you all for their love and support.

Contents

Contents vii

List of Figures ix

List of Tables xi

1 Introduction 1
- 1.1 Importance of metals as energy carriers . . . 1
- 1.2 Research goal . . . 2
- 1.3 Thesis outline . . . 3

2 Background 5
- 2.1 Aerosol combustion . . . 5
  - 2.1.1 Aerosol . . . 5
  - 2.1.2 Metal aerosol combustion . . . 5
- 2.2 Literature review . . . 6
  - 2.2.1 Iron aerosol combustion . . . 6
  - 2.2.2 Zinc aerosol combustion . . . 9
- 2.3 Characteristics of aerosol . . . 10
  - 2.3.1 Dynamic behavior of aerosol . . . 10
- 2.4 Characteristics of Micro Metal Dust Burner . . . 12
  - 2.4.1 Top plate preheating system . . . 13

3 Optimization of the Burner Setup 15
- 3.1 Lower electrode optimization . . . 15
- 3.2 Top plate assembly . . . 16
- 3.3 Preheating system . . . 17
  - 3.3.1 Inline preheater . . . 18
  - 3.3.2 Mica preheater . . . 20

4 Particle Velocity Analysis 27
- 4.1 Photographic device . . . 27
- 4.2 PTV analysis . . . 28

5 Number Density 31
- 5.1 Number density estimation . . . 31
- 5.2 Terminal settling velocity . . . 31
- 5.3 Experimental approach . . . 33
- 5.4 Optical size determination . . . 38

6 Investigation of Zinc Metallic Aerosol **43**
6.1 Combustability of Zinc aerosol 43
6.1.1 Flammability test in preheated burner system 43
6.1.2 Flammability test using burner without preheating 45

7 Conclusions **49**

Bibliography **51**
.1 Laboratory Setup and Technical Specifications 55
.1.1 Heating element 56
.1.2 Optical Analysis 57
.1.3 Cooling Channel in Top electrode 57
.1.4 Safety instructions 57
.2 Preheating 60

List of Figures

2.1 Model of single iron particle combustion [1] . . . 7
2.2 2D midsection view of burner's basic working principle with parts labelled [2] . . . 12
2.3 Burner with simple top electrode without preheater [2] . . . 13
2.4 Upper electrode assembly view . . . 13

3.1 Lower electrode new design (sizes are in mm) . . . 16
3.2 Upper electrode assembly, section view . . . 16
3.3 Upper electrode view . . . 17
3.4 Preheating elements . . . 18
3.5 Inline preheater insulated with glass wool . . . 18
3.6 Temperature measurement positions of the air flow from inline preheater . . . 19
3.7 Temperature of the preheated shroud flow gas . . . 19
3.8 Block diagram for the LabVIEW interface for temperature measurement . . . 20
3.9 Temperature of the preheated shroud flow gas (Thermocouple at the centre of the top plate) . . . 21
3.10 Temperature measurement positions of the air flow from the top electrode . . . 22
3.11 Temperature of the preheated shroud flow gas (Thermocouple at 5 mm from the centre of the top plate) . . . 22
3.12 Temperature of the preheated shroud flow gas with increased power (50 W) to heating element (Thermocouple at the centre of the top plate) . . . 23
3.13 Temperature of the preheated shroud flow gas with increased power(50 W) to heating element (Thermocouple at 5 mm from the centre of the top plate) . . . 24
3.14 Temperature of the preheated gas flow gas (central jet and shroud flow) at different heights (Thermocouple at the centre of the topplate) . . . 24
3.15 Temperature of the preheated gas flow gas (central jet and shroud flow) with variable voltage controller (Thermocouple on the heating element and 1 mm above the topplate) . . . 25

4.1 Flame images of carbonyl-iron powder burning in air . . . 28
4.2 Experimental setup with devices labelled with letter . . . 28
4.3 PTV image evaluation by PIV View using Pentacon lens for a jet height of 1.5 cm with an exposure time of 12 ms . . . 29
4.4 PTV image evaluation by PIV View using Naviator lens for a jet height of 6 mm with an exposure time of 22 ms . . . 30
4.5 PTV image evaluation by PIV View using Navitar lens for a jet height of 6 mm with an exposure time of 22 ms . . . 30

5.1 Terminal settling velocity of the particle in fluid flow . . . 32
5.2 Stable zone of the aerosol cloud where ignition occurs. Image taken using Naviator lens during iron aerosol dispersion using M^2DB . . . 33
5.3 Experimental setup for capturing the metal particles . . . 33
5.4 Filter holder parts (left) and PVDF membrane disc(right) . . . 34

5.5 Particles collected over the edge of the membrane filter 35
5.6 Combusted iron particle collection using filter 35
5.7 Combusted iron products captured in the membrane filter(grey oxides are magnetite and yellow or reddish brown oxides are hematite) 35
5.8 Number density and Mass aerosol density profile over time period 37
5.9 Red iron oxides (Hematite) near the iron flame front 37
5.10 Iron oxide samples in the petridish for microscopic analysis with number indicated for two different oxygen concentration and height 38
5.11 Optical microscopy images of sample collected near flame zone (21 % oxygen) . . . 39
5.12 Optical microscopy images of sample collected at a height of 10 *cm* from flame zone (21 % oxygen) 40
5.13 Optical microscopy images of sample collected near flame zone (60 % oxygen) . . . 40
5.14 Optical microscopy images of sample collected at a height of 10 *cm* from flame zone (60 % oxygen) 41
5.15 SEM images for sample of combusted iron powder 41

6.1 Effect of zinc flame propogation towards the aerosol exit 44
6.2 Burner without preheating system of central jet area of top plate with 3.14mm^2 . 47

1 Gas supply board 55
2 Labview interface for shroud flow control. A change in setpoint of 10 to 20 *cm/s* and back to 10 *cm/s* is shown 56
3 Technical drawing for the new capacitor (lower electrode) 58
4 Technical drawing for the top alunium casing for top plate 59
5 Position of the thermocouples at Top plate gas exit for Temperature measurement of the preheated gas flow gas 60
6 Temperature of the preheated gas flow gas (central jet and shroud flow) at a height of 1 cm)(Thermocouple at the centre of the topplate) 61
7 Temperature of the preheated gas flow gas (central jet and shroud flow) at a height of 2 cm)(Thermocouple at the centre of the topplate) 61
8 Temperature of the preheated gas flow gas (central jet and shroud flow) at a height of 3 cm)(Thermocouple at the centre of the topplate) 62
9 Temperature of the preheated gas flow gas (central jet and shroud flow) at a height of 4 cm)(Thermocouple at the centre of the topplate) 62

List of Tables

3.1 MFC details used for 0.785mm^2 15

5.1 Number Density estimation from mass of captured particles 36
5.2 Number density estimation of iron particles with and without combustion 36

6.1 Zinc powders used for experiments 43
6.2 MFC details used for increased central jet flow area (3.14mm^2) 46

1 Trigger output signal types used for PIV analysis 57

Nomenclature

Symbol	Meaning
$\dot{m}_o$	Mass consumption rate of oxygen per unit area
T	Temperature
P_o	Pressure of oxygen
R	Universal gas constant
E	Activation energy of oxygen atoms in the oxide layer
s	Surface area of the molten oxide
t	Burn-out time
b	Mass required for oxidation of iron per unit mass
R_o	Initial radius of iron particle
ρ	Iron density
s_o	Initial surface area of the iron particle
$\dot{m}_{oo}$	Initial oxygen mass consumption rate
d_m	Measured minimum diameter
d_g	Geometric mean diameter
σ_g	Geometric standard deviation
d_p,D_p	Diameter of the particle
F_d	Drag force or frictional force
μ	Dynamic Viscosity of gas
u_p	Particle velocity
v	Kinematic viscosity
Re_p	Reynolds number
ρ_g	Gas density
ρ_p	Particle density
C_c	Cunningham slip correction factor
Kn	Knudsen number
F_g	Gravitational force
R	Radius of the particle
V_t	Terminal settling velocity
v, V	Air flow velocity
g	Acceleration due to gravity

Chapter 1

Introduction

In this thesis, the aerosol characteristics of a micro-sized metal dust burner will be discussed. The focus of the project was to analyze the characteristics of the aerosol jet in two different conditions: with preheating and without preheating the aerosol jet. The metal powders investigated in this research were iron and zinc. The experimental setup enables the research of metal aerosol powders to find its fundamental characteristic properties such as particle velocity, number density, etc.. Moreover, the investigation of captured combusted iron was carried out using optical and scanning electron microscopes. This introduction addresses the importance and potential aspects of metal fuels. Second, the necessity of finding the fundamental properties of the aerosolized flame and the scope of the research are explained. Finally, the thesis outline is presented.

1.1 Importance of metals as energy carriers

Global consumption of fossil fuel continues to increase rapidly over the past few years. Most of our current uses of fossil fuels are related to high-energy applications, like transportation and energy production. Crude oil reserves are vanishing at the rate of 4 billion tonnes a year [3]. If this consumption rate remains, with no increase in population growth, fossil fuels like oil, gas and coal will be depleted by 2088. On the other hand, CO_2 emission is increasing gradually over the years which contributes to global warming. According to the statistical review of World Energy 2015, published by British Petroleum (BP P.L.C.), emissions in Asia Pacific countries are around 35000 million tonnes of CO_2 in 2015 which is twice the emission level in 1965 [4]. With the Paris Agreement, 174 countries and the European Union signed an agreement to reduce greenhouse gas emission and to do their best to keep the global warming well below 2°C. Among these countries, China, India and the United states are the three largest contributors of greenhouse gas emissions. Since fossil fuels are unsustainable, environmentally destructive and primary contributor to global climate change [5], the need for an alternative source to replace fossil fuel has become a major issue throughout the modern industrial economy over the past few years.

Nuclear and renewable energy such as solar, wind, geothermal and hydroelectric energy are used for replacing fossil fuels. Renewable energies derived from wind, sunlight and water depend on weather, and changes in weather makes the resources unpredictable and inconsistent. Thus, it has major disadvantages in-terms of reliability of supply. Moreover, it is very hard to store and transport the energy produced by renewable sources from one place to another. Cost of renewable energy technology is also far in excess as compared to fossil fuel generation. This is because the renewable energy technology is new and requires high cost to set up. In order to tackle these issues, other proposed solutions are low carbon energy carriers such as biomass, batteries and hydrogen to replace fossil fuels. But they also have many disadvantages in terms of production and usage. Biomass energy is harmful to the Earth ozone layer as they release methane which is as worse as CO_2 [6]. Moreover, the amount of energy produced by biomass is inefficient as compared to fossil

fuels. Batteries are a fairly safe option, but energy density is quite poor and they are too heavy. While hydrogen energy density is higher, it is flammable and volatile, thus making it dangerous to store and transport. Therefore, the need for another kind of fuel that fulfills desires such as energy density, low cost and ready availability for energy production like fossil fuels has become great importance.

Metals and specifically metal powders are a promising group of energy carriers with zero-carbon recyclable fuel option, although they are largely overlooked by scientists and researchers [7]. Metals react energetically with oxygen in air to form metal oxide, a non-toxic reaction product that can be collected and recycled. The energy densities of metal oxides are higher than gasoline or any other fossil fuels, which can be used as a standalone fuel for direct combustion process. Redox reactions of metal oxides have to be very well studied for efficient recycling to metal powders as this has been largely overlooked by scientists in the past few decades. The idea of burning metal powder is nothing new, since it has been used in military and aerospace applications from the mid-20th century. For instance, boron and aluminum are potential fuel additives in rocket propellants and explosives [8–11]. The combustion properties and the explosive limits (for safety concerns) of metals such as hafnium, magnesium, zinc, titanium, aluminum, iron, niobium, tungsten, boron, copper and lead were investigated in the past decades for possible use of metals as energy carriers [12].

The redox reactions of metal oxides are an important concern in the research of metal fuels. It is because they have environmental impact during conversion of metal oxides to metals. In particular, hydrogen and carbon are most widely used reducing agent in the process [13]. Iron powders are considered as primary metal fuel according to the study of McGill researchers, since there are already million tons of iron powders produced for the metallurgical, chemical and electronic industries [7]. Therfore, Iron can be considered as the large scale energy source of the future [14].

1.2 Research goal

Although few investigations on the metal aerosol combustion have been carried out in the past, the combustion mode of metal particles and its combustion properties are still in the dormant phase. Studying the different combustion modes, products formed and recycling of the metal aerosols are increasingly difficult. For understanding the combustion behavior of metal aerosols, individual particle interactions should be known. Experimental results [15–19] obtained over the years in similar methods yielded a wide range of particle behavior. Particle size, distribution, temperature and purity of the metal aerosols had a major influence in the experimental results [20]. This uncertainty results makes it difficult to develop a uniform model for understanding the metal particle dispersion and combustion.

For better understanding the metal particle dispersion and combustion, a metal particle (suspension) burner had been developed at Eindhoven University of Technology. This burner uses high voltage dispersion to levitate metal particles between the electrodes [2]. The goal of the project is to optimize the burner and investigate the characteristics of the aerosol jet. It involves adding preheating system and optimizing the burner by analyzing the temperature profile of the gas flow. Later with a stabilized jet, characteristics of the jet such as particle velocity and number density are evaluated with experimental results. The methodology involves tracing the particles in the aerosol jet. Using the burner, an aersol jet is directed vertically up, and decelerating in a stagnant flow surrounding the jet. The project involves four phases to determine the characteristics of the metal aerosols. First, the metal-air(iron) aerosol jet is investigated for particle velocity analysis using optical method. Second, the jet is preheated at different temperature and optimized. Third, the metal-air aerosol (iron) jet number density is investigated and results are discussed. Finally, the metal-air aerosol jet (zinc) is preheated at different temperature and oxygen concentration, its combustablity is experimented. The number density of the metal aerosol in the jet is measured

using a simple method by capturing the metal oxide. Since the burner apparatus is designed for different operating conditions, a comprehensive study which involves particle concentration, oxygen concentration and temperature of the jet is performed and analyzed.

1.3 Thesis outline

In the first section of Chapter 2, Backgound, a review of metallic aerosol combustion. The second section is about the literature review of iron and zinc aerosol combustion which is used as metal aerosols in the experimental study. The third section of this chapter focuses about the characteristics of the aerosol. The final section involves an overview of the micro metal dust burner and its top plate preheating system is explained. Since the new burner design is not a relatively new subject in our research group, a detailed overview is not given for the burner design.

The experimental setup is explained in the Chapter 3, Optimization of the Burner and the preheating setup. The optimization of the burner based on powder consumption is increased, by a new lower capacitor plate. Then, the preheating setup of the burner setup is discussed briefly in this section. It involves two different heating systems, mica heating element and an inline preheater. The efficiency of the heating systems with temperature controllers are tested based on the heat flow measurements. The preheating system is optimized during the investigation and the results are discussed in this section.

Chapter 4, Particle Velocity Analysis, gives an overview of characterization of particle velocity in aerosol jet. The experimental setup is discussed clearly for the optical analysis. Using optical diagnostic technique (PIV analysis), the experimental data of the metal-air aerosol jet is recorded, analyzed and the results are discussed.

Number Density of iron particles in the aerosol jet is discussed in Chapter 5. It gives an overview of the measuring the number density of metal particles in the aerosol . Using a simple setup, the particles of iron and iron oxides are captured using an filtration element and the number density is estimated in the aerosol flow. Finally, the captured particles are analyzed in optical microscope and scanning electron microscope, and the inference of the microscopic analysis is discussed.

Followed by iron combustion, Investigation on zinc aerosol combustion in the metal dust burner is briefed in the Chapter 6. Since, zinc requires preheating to react with oxygen, several tests are carried out to burn the zinc aerosl on various conditions using the metal dust burner. Finally, Conclusions are given in the Chapter 7, based on the results obtained during the test from the apparatus. Some recommendations are given for other possible study of the flame characteristics of the metal aerosol.

Chapter 2

Background

This chapter gives an overview of several topics related to metal aerosol combustion and metal dust burner. First section involves the research activities carried out in metal aerosol combustion. The second section is about the literature study related to iron and zinc aerosol combustion. And the third section includes the dynamic behavior of aerosol during suspension. Finally, the micro metal dust burner working principle is shortly outlined along with the preheating top plate design.

2.1 Aerosol combustion

2.1.1 Aerosol

Aerosols are suspensions of solid or liquid particles in a gas (usually air). Though the term aerosol was first presumably used by Frederick G.Donnan during World War I , aerosol package (cannisters with propellants) has been a subject of interest during World War II [21]. Aerosols are classified based on their physical forms as, dust, fume, mist, smoke and fog. In that classification, dust, fume, and smoke are solid-particulate aerosols. Dust is formed by mechanical disintegration of a parent material (fragmentation or resuspension) which is generally $1 - 100$ μm diameter. Fume is produced by condensation of vapors or gaseous combustion products, the condesate size is usually less than 1 μm. Smoke is a visible aerosol produced from incomplete combustion containing particle sizes between $0.01 - 1$ μm.

2.1.2 Metal aerosol combustion

The combustion of metal particles suspended in a gaseous flow is referred to as dust or suspension combustion. These aerosol undergo multiphase combustion including homogeneous (via vapor phase) or heterogeneous (via particle surface) combustion reactions. When a mass of solid flammable metal is heated in air, the metal burns slowly as the surface area exposed to the oxygen in the air is limited. If the mass of the same metal is reduced to fine powders and mixed with air and combusted, the aerosol burns rapidly. Because of the greater area exposed and the ignition is faster.There is a range of dust concentration in a mixture of air and dust that can explode when burning, but this is not the case with all mixtures. At concentrations above or below this range, the aerosol cannot explode. This upper and lower limit concentrations, which is capable of exploding are named upper and lower explosive limits. There are several instances of dust explosions in the past, which resulted in investigation of metal aerosol combustion for both safety [22] and energetic use of metals [23] [24].

Coal is one of the most combustible element. Even though coal is a high variable substance, extensive research has been done to understand the characteristics of coal combustion. Coal, being a complex mixture of partly volatile hydrocarbons, it is complicated to study the fundamental characteristics of combustion reaction. On the other hand, metals are combustible elements with

uniform composition. Study of metal explosion properties offer fundamental insights to combustion mechanism, despite its discrete phase transitions and vaporization behavior [12].

2.2 Literature review

Hertzberg et al. [25] discuss the fundamental issues of reaction mechanisms of dust flames which proceed either homogenously or heterogenously. Data were reported for 14 metals which includes volatile metals (zinc and magnesium), refractory metals (tantalum, tungsten and niobium), intermediate metals (hafnium, titanium, aluminum, iron, lead and copper) as well as non-metallic elements (boron, silicon and carbon). The data were analyzed in terms of calculated adiabatic flame temperature and equilibrium or non-equilibrium vapor fumes at those temperatures. The analysis resulted in the conclusion that volatile metals follow homogenous reaction. However, the issue of free flame propagation in heterogenous reaction phase remained unresolved. They also recommended to avoid excessive emphasis on single particle mesurements, as that had little relevance to conditions in freely propagating aerosol flames.

2.2.1 Iron aerosol combustion

Various studies of fundamental causes and prevention of losses by dust explosion have been performed in the last few decades [26]. These studies were carried out in closed experimental chambers to find measurement quantities in dust explosions such as explosion pressure, rate of pressure rise, explosion temperature, minimum ignition energy, and explosion limits. However, few studies had been conducted to find flame propagation mechanisms and structure of combustible aerosol clouds. Sun et al. [27] investigated the behavior of iron aerosols during flame propagation. The iron particle diameters are a few micrometers, ranging from 0.5 to 8 μm. In their apparatus, particle were blown in with pressurized air and ignited by an electric spark (for a duration of 30 ms), after which the self propagation of the flame was recorded on photomicrographs using a high speed video camera. It was concluded that the combustion mechanism was heterogenous with a flame zone of 3 - 5 mm in width. The velocity of flame propagation was almost constant, whereas the flame velocity depends on the particle size and cloud concentration.

In one of their successive studies [1], the burning behavior of individual iron particles in the combustion zone was examined in detail. The diameters of the particles were distributed mostly from 1 to 3 μm for iron particles (1), from 2 to 4.5 μm for iron particles (2). For iron particles (1) with a fixed concentration of 790 g/m^3, the flame propagates spherically after 40 ms with almost constant velocity. For iron particles (2) with a fixed concentration of 1050 g/m^3, the combustion can be identified as the movement of a luminous zone which consists of luminous particles (burning iron particles). However, the velocity of the burned particles were not constant but decreases from the leading combustion zone. After a height of 3.5 mm from the leading edge of the combustion zone, the burning iron particles change their direction of movement from upward to downward. Furthermore, the average diameter of the burned iron particles was larger than that of the unburned ones. This increase in diameter was the result of oxidation of iron particles. The density of iron oxide was smaller than that of iron, whereas the mass of each particle increases. The average diameter of iron oxides agrees fairly well with diameter distribution calculated on the basis of measured unburned particle diameter. A few particles of much larger diameter were inferred to be caused by agglomeration.

The combustion mechanism of solid iron burning in pure oxygen have been studied by Hirano et al. [28], 1994, [29], 1993; Sato et al., 1983 [30]. They proposed a model of the iron oxidation process during combustion. In their model, an oxygen consumption rate $\dot{m}_o$ is used to express the oxidation reaction rate of iron [28].

$$\dot{m}_o = C P_o^n T^m \exp(-\frac{E}{RT}) \tag{2.1}$$

In equation 2.1 where C, n, and m are constants. T is the temperature, P_o is the pressure of oxygen, R is the universal gas constant, E is the activation energy of oxygen atoms in the oxide layer, and $\dot{m}_o$ is the mass consumption rate of oxygen per unit area at molten oxide surface. According to their model and experimental results of this study, the combustion of an individual iron particle can be described in fig 2.1. In the case of a spherical single iron particle, the equation representing the mass balance at the particle surface is given by,

$$\int_0^t \dot{m}_o s \; dt = b\frac{4}{3}\pi R_o^3 \rho \tag{2.2}$$

Where, s is the surface area of the molten oxide, t is the burn-out time, b is the mass required for oxidation of iron per unit mass, R_o and ρ are the iron particle initial radius and iron density, respectively in the equation 2.2.

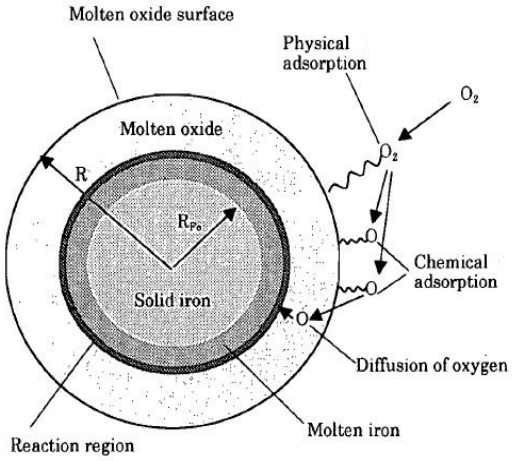

Figure 2.1: Model of single iron particle combustion [1]

The oxygen mass consumption rate and surface area of molten oxide varies during combustion. $\dot{m}_o s$ is approximated to a constant value, and is considered equal to $\dot{m}_{oo} s_o$ ($\dot{m}_{oo}$ is the initial oxygen mass consumption rate, s_o is the initial surface area of the iron particle). Equation 2.2 can be written as,

$$t = \frac{4b\pi\rho R_o^3}{3 s_o \dot{m}_{oo}} \tag{2.3}$$

Equation 2.3 means that the burn-out time of an individual iron particle is almost proportional to its initial volume. Thus, the larger iron particles have longer burn-out times which was also observed in the experiments [1]. The burn-out time of the iron particle was determined by the duration of its light emission, and its diameter was determined by direct measurement of the luminous point. They also inferred that the luminous point diameter before the combustion zone, which is a non-combusted iron particle, was few times larger than that of the unburned particle measured by scanning electron microscopy. This might be due to an aberration effect of the optical system. As this measured diameter near the luminous point has to be proportional to its initial diameter of the iron particle, according to the geometric optics theory [31], a non-dimensional diameter d/d_m (d is measured diameter and d_m is the measured minimum diameter) was introduced. From that, it was concluded that if the particle diameter is not so large, then the burn-out time of iron particle was seen proportional to the non-dimensional diameter. In this case R_o in equation 2.3, is equal to the ratio of measured radius of the iron particle near the luminous point to the measured

minimum radius.

In another paper of Sun et al. [32], a linear relationship between propagation velocity and the maximum temperature of iron aerosol was found. The experimental results indicated that when the iron concentration increases, temperature increases to a maximum value and then decreases at higher concentration. The results also suggested that conductive heat transfer is dominant in iron aerosol flame propagation. Followed by that, in 2003 [33], the number density profile of iron cloud was studied. The measured number density changes, when it is measured at a distance x mm from the leading combustion zone. It was compared with the theoretical model, suggesting an increase in number density ahead of the flame, which appear not only for iron particle cloud but also for any two-phase combustion systems. In a successive paper [34], they discussed about velocity and number density profiles of particles across upward and downward flame propagation in iron aerosol cloud. In 2009, Tang et al. [35], studied the laminar flame propagation in iron dust clouds of size ranging from 3 - 27 μm in a parabolic flight aircraft under reduced-gravity condition. Inside a glass tube, a uniform dust suspension was created and ignited by an electrically heated tungsten wire. Flame propagation speeds were determined in both open tube and quenching plates. Flame quenching distance increased when iron particle size was increased from 3 to 27 μm. The experimental results correspond with the predictions of a theoretical model of one-dimensional dust flames with conductive heat loss, when it is assumed that the particle combustion took place in the diffusive regime . In a successive paper [36], they proposed so-called argon/helium test to identify different combustion modes of particles in iron flame. Particle size varied from 3 to 34 μm, were dispersed in argon and helium replacing nitrogen in air. Due to this replacement, the particle burning rate is independent of oxygen diffusion in kinetic mode, and the flame speed in He/Ar mixture is smaller. The mode of particle combustion was investigated by flame speed ratio between $He - O_2$ and $Ar - O_2$, maintaining constant thermodynamic and kinetic properties and varying thermal and transport coefficients. The resulting values for larger iron particles (squared ratio of flame speeds in helium and argon mixture = 5.3 - 7.7) were in agreement to the theoretical model assuming a diffusive mode of combustion, whereas, the values for finer iron particle (squared ratio of flame speeds = 2.7) implied the onset of a transition from diffusive to kinetic mode of particle combustion.

In the work of Poletaev et al. [37], the combustion products of Fe, Al, Zr, and Ti were characterized in terms of size. This characterization was subsequently related to combustion process, initial particle size and impurities. The size distribution of these metal oxides were in the range of 30 - 100 nm with a log-normal distribution. Iron aerosol gas-phase combustion was reported along with its combustion temperature and boiling point. Measured combustion temperature of iron is lower than its boiling point and the products formed in this case, are close to the size of initial iron particles. The results obtained for gas-phase combustion at these temperatures stated that intermediates were formed contradicting to the statement given by Wright for iron dust combustion [38]. Bidabadi and his fellow researchers contributed to the development of models for iron dust combustion. Haghiri and Bidabadi [39] analyzed the dynamic behavior of iron particles across flame propagation through a two-phase mixture consisting of micro-iron particles and air. First, a Lagrangian approach was used to calculate the particle velocity profile. Later, thermophoretic, gravitational and buoyancy forces were taken into consideration. The results show that thermal radiation of iron particles helps in increasing the combustion temperature all over the preheat zone, were consistent with the experimental model data. Further, this research group studied the flame front propagation of micron-sized iron dust particles in a vertcial duct [40] and in media with spatially discrete sources [41].

Microsized iron particles are not easily burnt in ambient conditions at low concentration. Thus iron suspension was investigated, in reduced gravity and normal condition, with methane assisted combustion at McGill university. Julien et al [42], investigated the particle concentrations in the range of 0 - 350 g/m^3 in both stoichiometric and fuel lean methane-air mixtures in a modified bunsen burner. The reaction is controlled by kinetic regime for hot combustion products

in stoichiometric condition, resulting in slow iron oxidation. Moreover, the iron flame front in the kinetic regime, forms only after a critical particle concentration. For some critical mass concentration, the iron aerosol in methane-air mixture had a double flame front seperated by dark zone (where there is no flame). For fuel lean mixtures, iron particles react with excess oxygen in the diffusion controlled regime and the flame appears like a single bunsen cone. Silicon carbide particles were also added to the same mixture for comparison. The iron flame temperature in excess oxygen concentration were close to the adiabatic flame temperature of single iron particle combustion. The temperature in the diffusion controlled regime was about 400 K higher than in the kinetic controlled regime and almost equalled the adiabatic flame temperature of methane.

2.2.2 Zinc aerosol combustion

Burning zinc containing precursors is one of the important steps in the synthesis of zinc oxide, which is used in various applications including LEDs, transparent transistors, solar cells, memory devices, rubber manufacturing, ceramic production, desulfurization processes, cosmetics, medical and dental products [43]. Zinc reacts with oxygen to form zinc oxide, an exothermic reaction which release heat that can be utilized. In this process, additional energy is required from an external source, for zinc vaporization. Derevyaga et al. [44] conducted experiments with zinc and aluminium under two conditions. First, the sample was burnt with a hot air stream flowing with a velocity of 15 - 20 cm/s. Second, the sample was heated up in an inductor and air (at atmospheric temperature) was blown over it. For zinc, it was concluded that both the ignition and combustion of the sample does not depend on the method of heating, it was determined by the temperature of the sample. If the sample temperature exceeds ambient temperature, then it is a complete combustion. Otherwise, the combustion fades and the sample is only partially burnt. Combustion products of zinc appeared to be needle-shaped formations with sizes more than 3 μm, indicating that the reaction takes place on the metal surface and surrounding gas around the metal.

In 2015, Rackauskas et al. [45] proposed a novel continuous method of burning micro-sized zinc particles in air to synthesize zinc oxide tetrapod (one dimensional zinc oxide nano-microstructure with multifunctional applications in varius fields). In their study, a vertical flow reactor was constructed to control and observe the process. This setup can control the ZnO-T$_s$ (zinc oxide tetrapods) final geometry and to find the main factors affecting the synthesis at high rates. The process involves heating the zinc particles. When they reach the melting point of $420°C$, the zinc melts and vaporizes. The vaporized zinc reacts with O_2 to form supersaturated zinc oxide vapor. Homogenous nucleation occurs in the ZnO nuclei which on further supply of zinc and oxygen help in zinc oxide crystal growth. The rate of Zn and O_2 supplied controls the ZnO crystal structure. When the zinc molecule supply was more than their diffusion to the ZnO crystal surface, the shape formation is controlled by kinetic control regime for highly anisotropic shape formation. For continuous $ZnO - T_s$ formation, increased amount of vaporized zinc with oxygen molecule is supplied. Otherwise it will result in a thermodynamically controlled process. In this case, the time taken for diffusion of ZnO on the surface of growing crystals would be high, resulting in formation of spherical nanocrystals. In this reactor, the critical temperature required for ZnO-T synthesis was 720°C. Lower temperature caused non-self sustaining combustion of zinc oxide due to low Zn vapor pressure and low O_2 splitting rate. This crystalline formation consists of four elongated structures with an average diameter of 15 $\pm$ 5 nm and a length of 200 $\pm$ 100 nm.

Later Poletaev et al [46], discussed the application of gas-dispersed (propane and air mixture) synthesis for production of zinc nano-particles. In particular, N.I. Poletaev started his research work towards the investigation of metal dust flame since 2007. This paper [46], also involved zinc oxide burning in a gas suspension. Two flames were identified based on the mixture and the oxidizer. First, laminar based premixed dust flame (LPDF) in which the oxidizer carries the metal particles in the oxidizer. Second, Laminar diffusion dust flames (LDDF), where the fuel was dispersed in an inert gas which burn within the accompanying flow of oxidizer. It was found that effect of heat on zinc was low when it react with oxygen, which makes it less reactive. From the

first method, the product formed were nanorods with length of 90 $\pm$ 10 nm, which was several times larger than transverse sized products (35 $\pm$ 10 nm). In the second method, half of them were tetrapods ($200 - 300$ nm which were needle like structures) and other half were nanorods (particle length of 300 $\pm$ 100 nm and diameter of 70 $\pm$ 40 nm). The propane concentration in LPDF and LDDF modes were 1.9 % and 2%. From the observation (under TEM) that ZnO particles formed seem to be hollow shells, concluding that heterogenous reaction did not occur in both regime.

2.3 Characteristics of aerosol

Characterization of metal aerosol is very important in order to understand the metal suspension behavior and combustion phenomena. Metal aerosol containing particles of uniform size are called monodisperse aerosols, whereas aerosols containing different particle sizes are called polydisperse aerosols. Most laboratory measurements use monodisperse aerosol for better test results. For polydisperse aerosol, a probability density function is used to characterize the distribution of particle sizes. The log-normal function fits well for most polydisperse aerosols. This distribution function is given in the following equation 2.4 [47].

$$f(d_p) = \frac{1}{\sqrt{2\pi} d_p \ln \sigma_g} \exp\left[-\frac{(\ln d_p - \ln d_g)^2}{2(\ln \sigma_g)^2}\right] \tag{2.4}$$

where, d_g and σ_g are the geometric mean diameter and geometric standard deviation, and d_p is the diameter of the particle in the aerosol. By definition, geometric mean diameter is the diameter of the particles which are largely present in the aerosol. This size distribution can most often be obtained using scanning electron microscopy (SEM) or transmission electron microscopy (TEM). Number concentration (number/cm^3) is one of the important parameter to be estimated for aerosol combustion characteristics. This estimate is necessary for finding the terminal settling velocity of the aerosol particle which is explained in the subsection 2.3.1. Investigation of chemical composition of the combusted aerosol particles contributes to its structural analysis and complex chemical nature of the aerosol during combustion [48]. This requires utilizing a series of optical analyzing techniques such as photoacoustic spectroscopy, laser induced incandescence methods, liquid and gas chromatography (LC and GC), X-ray fluorescence spectroscopy (XRF), and inductively coupled plasma-mass spectroscopy (ICP-MS).

However, there are various difficulties while employing optical techniques, which are aggregation and agglomeration of the aerosol during discharge. The particles and the gas molecules collide and stick to each other during dispersion; This is defined as coagulation or aggregation. This leads to decrease in concentration of the particles as they merge together which lead to diameter increase. Agglomeration is widely seen in metal aerosol, where the metal particles collide together during dispersion. The bond between the agglomerated particles are looser and easy to break.

2.3.1 Dynamic behavior of aerosol

The particle concentration in the aerosol will change over time due to internal and external processes. Internal processes involve nucleation, evaporation, condensation and coagulation. External processes that cause particle migration are diffusion, gravitational settling, electrical charging and so on.

Drag force

During aerosol dispersion in air, the resisting force of the surrounding gas molecules prevents the particles moving in air, which is defined as drag force. This drag force is governed by Stokes law. This law is valid only for spherical particles with small Reynolds number. For non-spherical

particles, the average diameter is assumed and Stoke's law is applied as an approximation. Drag force for a spherical particle is given by:

$$F_d = \frac{3\pi d_p^2 \rho_g u_p^2}{Re_p} \qquad \text{for } Re_p < 1.0 \tag{2.5}$$

In equation 2.5, F_d is the frictional force, μ is the viscosity of the gas, d_p is the diameter of the spherical object, u_p is the particle velocity during dispersion, ρ_g is the gas density and Re_p is the particle Reynolds number respectively. Reynolds number (Re_p) is a dimensionless number related to particle diameter (d_p), particle velocity (u_p), and kinematic viscosity of gas (v), expressed in the equation 2.6.

$$Re_p = \frac{d_p u_p}{v} \tag{2.6}$$

Reynolds number of the particle (Re_p) represents the ratio of inertial forces to viscous forces. When Re_p is less than 1, the inertial forces can be neglected. The drag force calculated from equation 2.5, has an error of 12% at $Re_p = 1.0$. The error decreases when particle Reynolds number (Re_p) decreases. One important assumption of Stoke's law is that the gas at particle surface has zero velocity relative to the particle [47]. This asssumptions holds well, when the particle diameter is larger than mean free path of the gas molecules. Mean free path is defined as the average distance travelled by a gas molecule between successive collisions. The interaction between the gas molecules and particles is better described by Knudsen number (Kn) . It is the ratio of mean free path to particle radius. When Knudsen number (Kn), is ≥ 1, then the dragforce calculated using Kn is smaller as compared to the drag force calculated by stoke's law. When the particle diameter is the same as the mean free path of the molecules, then the Cunningham slip correction factor (C_c) can be multiplied with the right side of equation 2.5. It is expressed in equation 2.7. This correction factor agrees well with experimental data for different particle sizes [49]. At ambient conditions, particle diameter is directly proportional to the absolute temperature and is inversely proportional to the pressure. Thus temperature rise results in increased slip correction factor (C_c).

$$C_c = 1 + Kn[1.257 + 0.4\exp(-1.1/Kn)] \tag{2.7}$$

Gravitational settling or Terminal settling velocity

As a result of balancing between gravitational force and drag force, the freely moving particle starts to settle at constant velocity, this is called terminal settling velocity of the particle which is given by equating gravitational force and drag force i.e. F_d=F_g. The drag force based on Stoke's law is given in equation 2.8 and the gravitational force is given in equation 2.9. By equating these equations, the terminal settling velocity of the particles is determined and is expressed in the equation 2.10. At this velocity (V_t), the particles settle to form a stable aerosol cloud and the flame occurs. This is the velocity of the particle before the flame zone.

$$F_d = 6\pi\mu R v \tag{2.8}$$

$$F_g = (\rho_p - \rho_g) g \frac{4}{3}\pi R^3 \tag{2.9}$$

$$V_t = \frac{2(\rho_p - \rho_g) g R^2}{9\mu} \tag{2.10}$$

From equation 2.10, ρ_p and ρ_g are the particle density and gas density, R is the radius of the particle, g is the gravity constant which is equal to 9.807 m/s^2, v is the air flow velocity and μ is the dynamic viscosity of gas respectively.

2.4 Characteristics of Micro Metal Dust Burner

The micro metal dust burner works on the principle of electrostatic dispersion. The powder is placed on the lower electrode which is connected to a high voltage source. A 2D mid section view of the burner system with parts labelled is shown in figure 2.2. The dispersion chamber is sealed with a grounded top plate which acts as an upper electrode (H). The lower electrode (A) is a cup-like design which acts as a powder reservoir. The charged powder gets directed through a small hole of 1 mm in upper electrode such that the dispersion in between the two electrodes does not enhance electric breakdown. The lower electrode is 55 mm in diameter and the cup should not be fully filled. The brim height of the lower electrode to the base of upper electrode can be set up to 4.5 mm. The height can be adjusted in such a way that the electric field intensity can be increased or decreased which has an effect on particle concentration. The dispersion chamber is a polycarbonate tube (G) of 53 mm height, which allows visual access of the dispersion between the electrodes. The base of the polycarbonate tube is connected to a base plate (E). Thus, the dispersion chamber is tightly sealed to prevent the air flow from outside of the chamber and keeping the system in an under pressure environment.

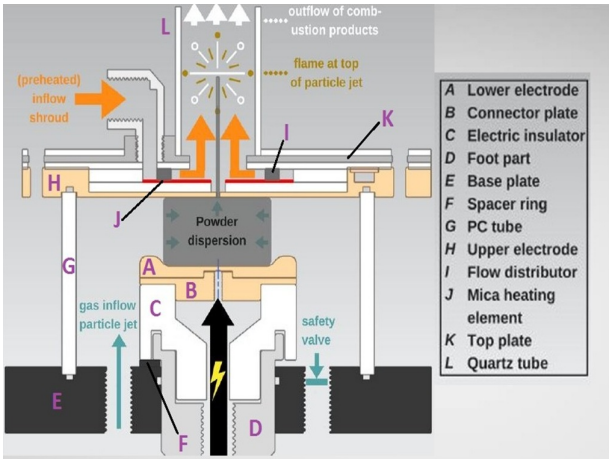

Figure 2.2: 2D midsection view of burner's basic working principle with parts labelled [2]

The lower electrode lies on the connector plate (B) which is connected to the high voltage wire. The part C is an electric insulator to prevent the voltage to pass on the chamber other than connector plate and lower electrode. The part J is the mica heating element (heater) to preheat the shroud flow. The flow inside the apparatus is a central jet which carries away the metal powder from the lower electrode through the 1 mm hole in the upper electrode. The shroud flow is supplied at one point in the top electrode which distributes the flow axisymmetrically using a porous element. This shroud flow envelops the central jet with metal powder to create a stable jet at certain height from the top plate. The upper electrode is a simple design comprising the shroud flow region with a porous ring to regulate the central jet. The top plate is sealed with the polycarbonate tube with a gasket in between. Then its is screwed with four threaded hole using winged nuts. The simple burner apparatus without preheater is shown in figure 2.3. It has a stainless steel plate (M) with an aerogel (O) placed above it . Later a porous ring over the top of the aerogel which is enclosed by a stainless steel casing (N) with an area for shroud flow to circulate and discharge through the porous ring. The top plate is sealed with a gasket (P) of 2 mm thickness. The metal particles loaded in the lower capacitor gets charged and leviated by the air flow inside the chamber, reaches the top stainless steel plate. It loses its charge and falls back due to gravitational force. The dense cloud created between the electrodes and the simple top electrode with parts labelled are also shown in figure 2.3.

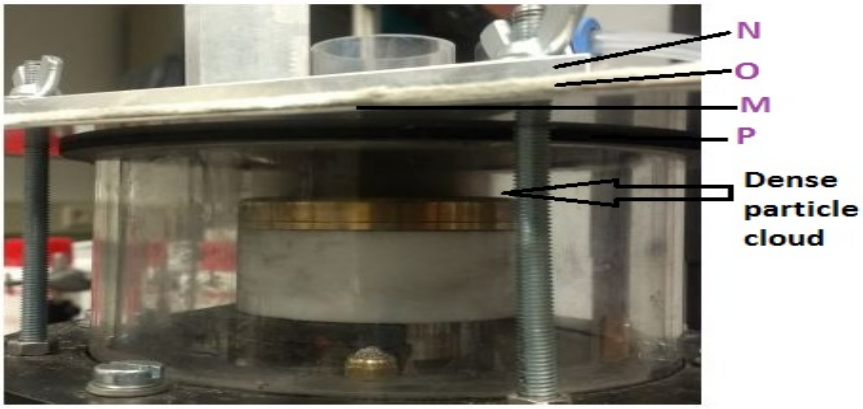

Figure 2.3: Burner with simple top electrode without preheater [2]

2.4.1 Top plate preheating system

The particles discharged in the burner system are preheated so that the flame front reaches higher temperature in the flame. This allows investigation of particle reaction during the combustion at different initial temperatures. The flow rate of shroud flow is higher as compared to the central jet, thus preheating the shroud flow is not much complicated. The upper electrode is made of copper for its high thermal conductivity. While preheating, it is important to prevent the heat transferred from the top elecrode to the dispersion chamber. For that, cooling channels with a width of 7 mm are made in the top electrode. Water circulates through the cooling channel which prevents the heat to transfer downwards from the top plate. The flow rate of the water is increased or decreased based on the set temperature of the heating element. The preheating system and its optimization are explained in the next chapter 3. From Figure 2.4 (a), the upper electrode bottom view is shown, where, the cooling channel is represented with a label D. While Figure 2.4 (b) shows the finished top plate electrode indicating A for the shroud flow and C is the mica heating element and D is the inlet or outlet for water cooling channel and B is the region where the shroud flow enters the porous ring creating an axisymmetric flow. Moreover, rubber stoppers (E) are used to prevent the leaking of circulating air in the shroud flow region.

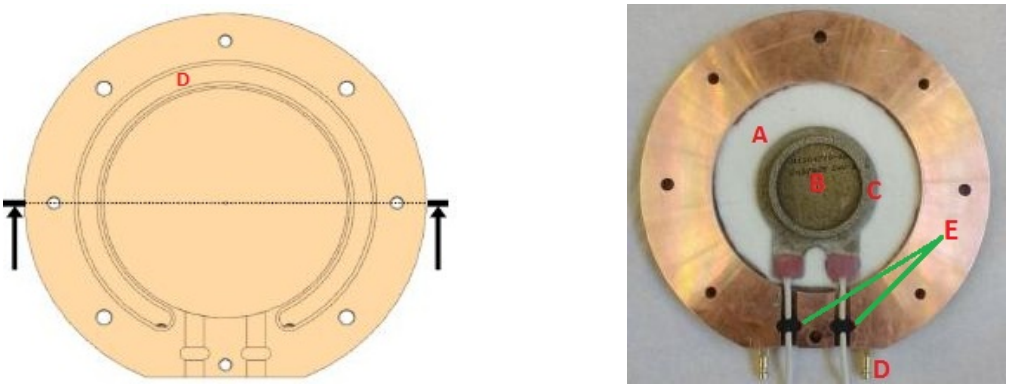

(a) Bottom view (b) Top view

Figure 2.4: Upper electrode assembly view

Chapter 3

Optimization of the Burner Setup

During dispersion, the metal powder from the lower electrode is not consumed efficiently as the charged metal particles fall around the lower capacitor. Preheating the air inside the top electrode needs optimal measures to prevent the heat loss inside the electrode using insulation materials. This chapter comprises of optimization of the burner in terms of efficient consumption of the metal powder in the lower capacitor and effective top electrode assembly. Later, the preheating systems and its efficiency in terms of temperature distribution using different voltage regulators are discussed.

The gas used in the experiments are oxygen and nitrogen, which are connected to the burner system using flexible polymer tubes from a gas supply board. Mass flow controllers control the flow rates of the gas and oxygen concentration, using a LabVIEW interface along with a NI-DAQ mx control system. Detailed information regarding the laboratory setup and information on operating gas flow and burner are described in Appendix .1. The diameter of the top plate orifice used during the test is 1 mm. For better understanding of the characteristics of the aerosol jet, the burner system has to be optimized as efficient as possible. A simple setup of the burner is shown in the figure 2.3. Table 3.1 shows the MFC details used for 0.785mm^2.

Table 3.1: MFC details used for 0.785mm^2

Central jet area 0.785mm^2				
	Central jet		**Shroud flow**	
MFC	1	2	3	4
MFC Number	MFC-30	MFC-40	MFC-33	MFC-9
Gas Used	Nitrogen	Oxygen	Nitrogen	Oxygen
MOB Port No	4	3	2	1
Max Flow Rate [Ln/min]	0.2	0.049	5.263	5.136

3.1 Lower electrode optimization

The metal powder gets charged from the voltage power supply and gets levitated using the gas flow inside the chamber. Through the 1 mm hole the particles are entrained through the top electrode with the gas flow, whereas the remaining charged particles which hit the neutral top plate loose their charge and fall down. During the particle levitation, particles in the brim area (indicated in figure 3.1) settle down on the base plate (Part E) i.e the area around the electric

insulator (Part C) as shown in the figure 3.2. This particle loss happens when the voltage is higher. When voltage is increased, the particle concentration in the flow also increases.

Inorder to reduce this particle settling inside the chamber at high voltage, the brim corner radius was increased from 2 to 4 mm and also, the height of the lower capacitor plate was increased from 6.5 to 7.5 mm. Additionally, the depth at the centre to hold metal particles was increased from 3 to to 4 mm. With the new design, as can be seen in the figure 3.1, the test was carried out. The increased depth enhanced capacity to hold metal particles and the particle loss around the brim corner had been reduced during high voltage. This was due to the inward pointing component of electric field which is reduced when the radius of the brim is increased. Thus the brim radius was doubled on comparison with the previous design. Increase in brim radius decreases the volume to hold the metal powder, its depth was increased by 1 mm. The specification sheet for the lower electrode can be seen in Appendix .1.

Figure 3.1: Lower electrode new design (sizes are in mm)

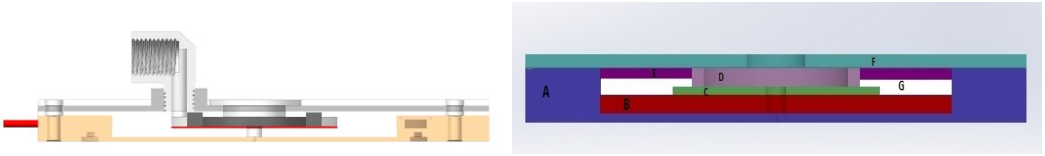

(a) Section view

(b) section view of central part of top electrode assembly

Figure 3.2: Upper electrode assembly, section view

3.2 Top plate assembly

A sectional view of the assembled upper electrode for preheating the aerosol jet is displayed in figure 3.2a and the parts are labelled in figure 3.2b. The components inside the top plate are explained in this section, with the parts indicated. The shroud flow area inside the top plate(**A**) initially amounts to 8.3 cm^2. Aerogel blankets were used in this shroud flow to prevent the heat transfer to the bottom or side of the copper plate. Four types of aerosol blankets were available for heat insulation. Although the standard aerogel blanket(**B**) of 3 mm thickness leaks some particles, it was decided to use this for the experiments, as it has high temperature resistance (650°C). As the temperature inside the top plate was planned to go upto 600°C, this standard aerogel was chosen. Two other aerogel blankets, aluminium and glassfibre cloth, also have high temperature resistance, but due to their thickness of 5 mm and stiffness, they are hard to fit in the top plate with heating element and porous ring enclosed. Since the impregnation aerogel has low temperature resistance (300°C), it was also not tested during the experiments. The aerogel material was cut to the same diameter as the shroud flow area, with a 5 mm hole at the centre. Above the aerogel material, a mica heating element (**C**) was placed, with its inner hole at the centre of the aerogel. The porous ring (**D**) was positioned on top of the heating element with an aluminium plate of thickness 2 mm over the porous ring.

Experiments were carried out in this top plate assembly without preheating to examine the stability of the jet. During some trials, the aerosol jet was unstable, and tends to incline sidewards. The reason for this inclination is that the porous ring moves off from the centre, when the top plate assembly is fixed. It was hard to determine the position of the porous ring when it was inside the top plate. Moreover, because of the small flow region, the shroud flow velocity is higher, causing the jet to become unstable. So, the shroud flow area (**G**) was increased from 8.3 cm^2 to 15.9 cm^2. Additionally, Isoplan Greenline 1000 material (**E**), an insulating material, was used to fix the porous ring at the centre. A hole of 43 mm (diameter of the porous ring) was made in the Isoplan 1000 which has a thickness of 2 mm where the porous ring was placed. This caused the porous ring to remain stable at the centre. This modification in the assembly enabled to achieve a stable jet. The aluminium top cover (**F**) has one inlet where the gas flow gets into the shroud flow region. Because of the increased area in the assembly for the gas flow, the inlet was positioned in such a way that it lies straight above the shroud flow region. The top casing with altered inlet is displayed in figure 3.3a. The closed assembly for the top electrode is shown in figure 3.3b.

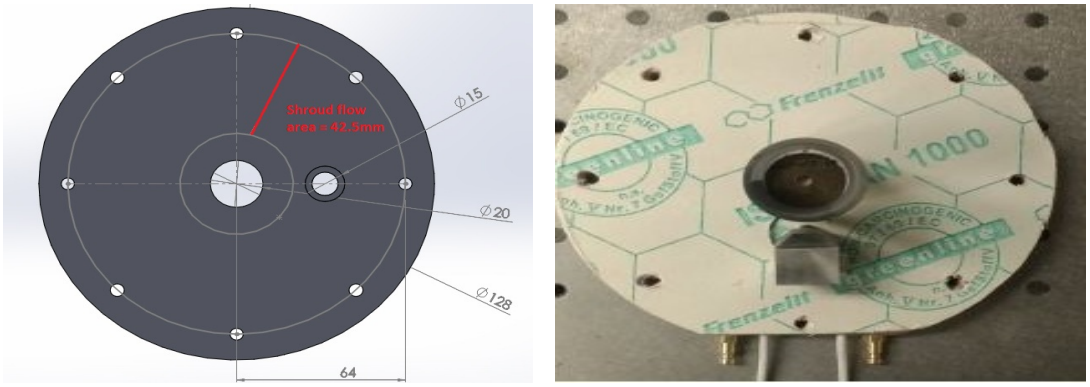

(a) Top plate aluminium casing

(b) Closed topview

Figure 3.3: Upper electrode view

3.3 Preheating system

The preheating system is designed to preheat the shroud flow gas. It is because preheating the shroud flow is less complicated than central jet and the volumetric flow rate is high. The flow area of central jet and shroud flow for a steady jet are 0.7850 mm^2 and 3.14 mm^2. Two preheating systems were tested, which were already available in the lab. One is the mica heating element ordered from Backer Calesco Sweden (M104718), which is assembled inside the top plate assembly. This mica heating element has a cental hole of 5 mm with the maximum voltage and power of 24 V and 190 W. It provides uniform heat distribution in the shroud flow region. Moreover, it can heat up and cool down in a short time making it very efficient in high temperature applications. This heating element consists of two mica sheets with a heating coil in between, which has a resistance of 3 ohm. The maximum temperature achieved by this mica heating element is around $800-900°C$ according to the data sheet. Because of its thickness of 2 mm, and compact structure as shown in figure 3.4a, it is suitable for top electrode preheating.

The other preheating element is the inline preheater ordered from Omega (AHP-7562). The shroud flow gas enters this preheater, heats up, and then enters into the shroud flow region inside the upper electrode and gets further heated using the mica heating element. This heater can preheat the gas flow up to 540°C. The inline preheater is shown in figure 3.4b. Both heating

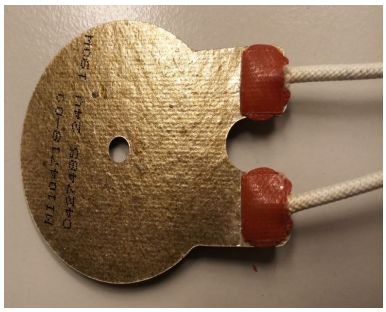

(a) Mica Heating element

(b) Inline preheater

Figure 3.4: Preheating elements

systems are controlled by two PID controllers, which get feedback from thermocouples connected to the heating units. The heating system is given power using the temperature controller and the input temperature is set in the controller manually. Based on the thermocouple feedback, the power given to the heating unit is increased or decreased. The thermocouple temperature and the required set temperature are displayed on the temperature controller. Further information about the optimization and usage of the preheating system are explained in the following subsections.

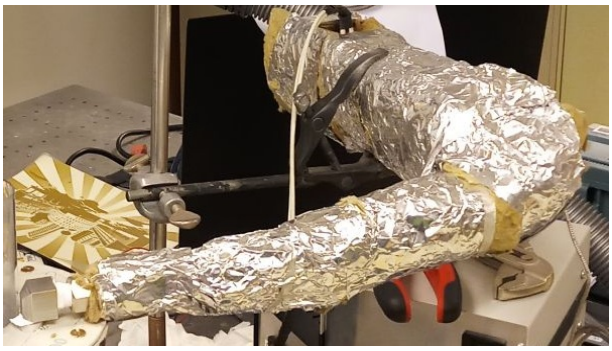

Figure 3.5: Inline preheater insulated with glass wool

3.3.1 Inline preheater

The inline preheater AHP-7562 with an approximate length of 280 mm, preheats the air by varying the voltage or air flow rate. It includes T-fitting (AHP-NPT34) for temperature sensor inlet and adds approximately 45 mm to the overall length of the heater. A K-type thermocouple (K-M-1-3-25-1/4NPT-GS-1) probe is used along with the T-fitting. It has a maximum temperature of 480°C with a 1 metre long glass fibre insulated lead connected to the temperature controller. The end of the fitting is connected to a stainless steel hose (from Witzenmann Hydra Gas) with insulation to resist temperature up to 400°C. The end of the gas hose is connected to the top aluminium plate connector. The suitable power supply for the inline preheater is 120 V or 240 V. The temperature controller with 120 V power supply was used initially. The minimum flow rate required for the preheating element to heat the flow efficiently is 29 litres/min. But the maximum allowable shroud flow gas velocity using the MFC is 25 cm/s which corresponds to 4.3 litres/min. Because of its low flow rate, the time taken for preheating was more than 60 minutes, if the temperature in the controller was set to 200°C. This delay in preheating is due to the power given to the heating unit. So, the power supply of the controller was increased to 240 V. The time taken to heat the airflow to 200°C was around 20 minutes. The thermocouple present after the heating

element measures the temperature of the hot gas and sends the feedback to the PID controller. The heating system is insulated with aerogel to prevent the heat transfer to the environment. Even though the temperature attained in the heating system was around 200°C, the temperature at the exit of the hose was only 28°C. It was due to the temperature loss in the heating system. So the heating system insulation was replaced with glass wool in such a way the whole heating element till the hose end is insulated, as shown in figure 3.5. The system was set to heat up at 200°C for more than 60 minutes, and the temperature is measured at two points using thermocouples, one at the exit of the hose (indicated as 2 in figure 3.6a) and the other at the exit of the top plate (indicated as 3 in figure 3.6b). The graph is shown in the figure 3.7.

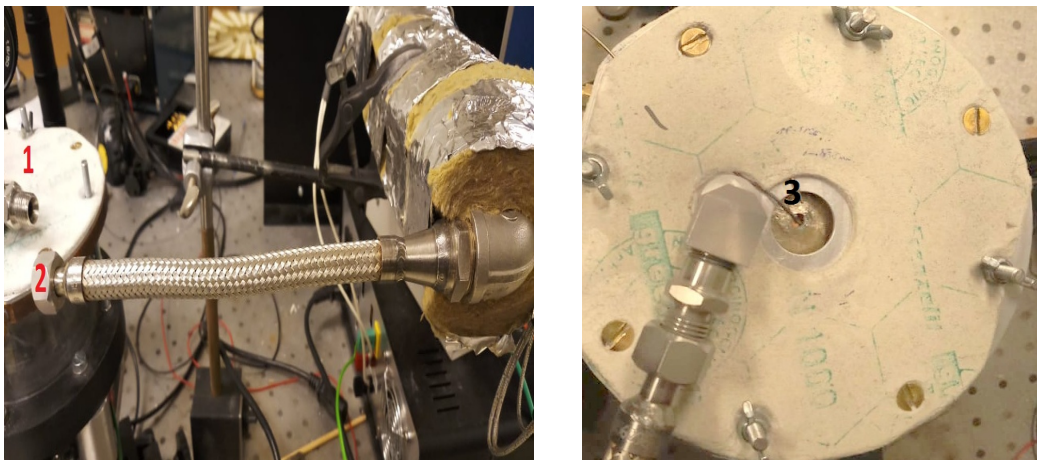

(a) Position 1 (b) Position 2

Figure 3.6: Temperature measurement positions of the air flow from inline preheater

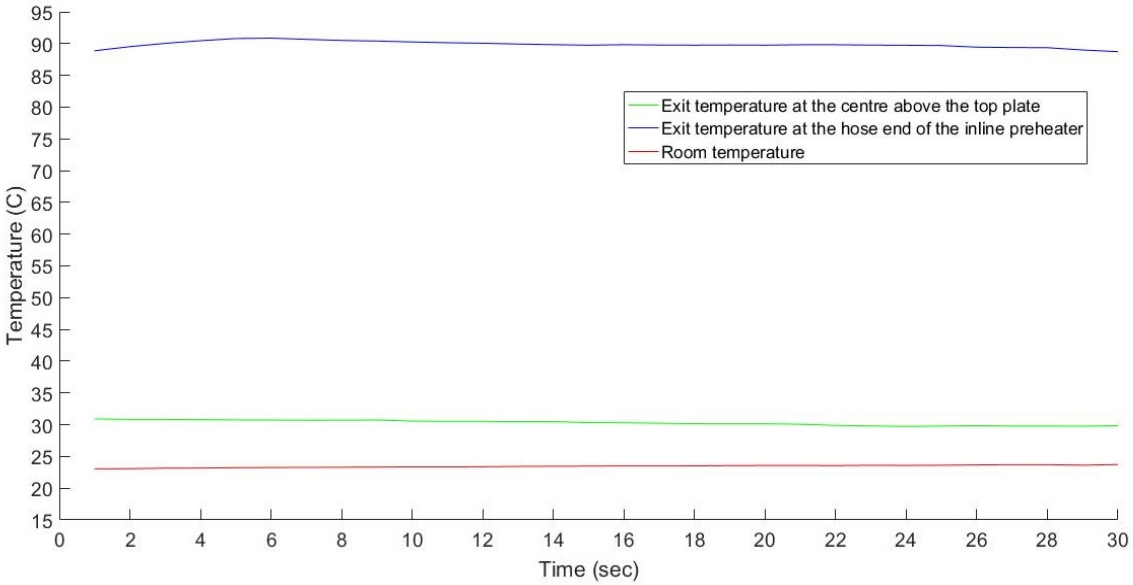

Figure 3.7: Temperature of the preheated shroud flow gas

The temperature remained 90°C at the hose end and 30°C at the exit of the top plate even after 90 minutes. There is still some heat loss taking place at the connection between the hose

to the inlet of the top aluminium plate (indicated as 1 and 2 in figure 3.6a). Moreover, the heat dissipation is high in the shroud flow area inside the top plate. The temperature obtained at the top plate exit is very small compared to the heater temperature. The inline preheater takes larger time to heat up and cool down. Thus, inline preheater is not efficient and time-consuming during heating and cooling. Further, the preheater was tested at high temperatures around 450°C. As the minimal flow rate for the preheater is 29 litres/min, the temperature inside the heater became high and the heater coil burnt inside. Thus, inline preheater to preheat the gas was inefficient when the gas flow has several connectors inbetween in which the heat loss occurs. In particular, the heat dissipation is very high around the top aluminium plate connector and metal hose end. When they were insulated tightly, the heat loss can be prevented but it affects while unmounting the top plate for reloading the metal powder. Moreover, gas flow rate is also considered in choosing these kind of inline preheaters.

3.3.2 Mica preheater

The assembly of the mica heating element inside the top plate is explained in section 3.2. This mica heating element is light weight with minimal thickness, and heats up instantly. It has a length of 6.65 cm and 28 cm long insulted wiring which is connected to the power supply. A thermocouple was placed on the top of the mica heater to measure the temperature of the heating element. A Watlow 935A PID temperature controller with transformer of 25 V and 4 A was used to control the temperature of the mica heating element. Inaccurate temperature measurements were achieved when the thermocouple was on the top of the heating element. This was due to the misalignment of the thermocouple on the mica heater when the top plate was assembled. Thus, the thermocouple was placed in between the aerogel blanket and the mica heater which holds it firmly and unmovable. Initially, the temperature set point in the controller was limited to 300°C, which was later changed to 1000°C by changing the internal settings in the controller. The heat loss inside the top plate is prevented by aerogel blanket and Isoplan 1000. Another layer of Isoplan 1000 placed on top of the aluminium plate restricts the heat transfer from the aluminium plate. This insulation holds the heat dissipated from the mica heating element and preheat the shroud flow gas.

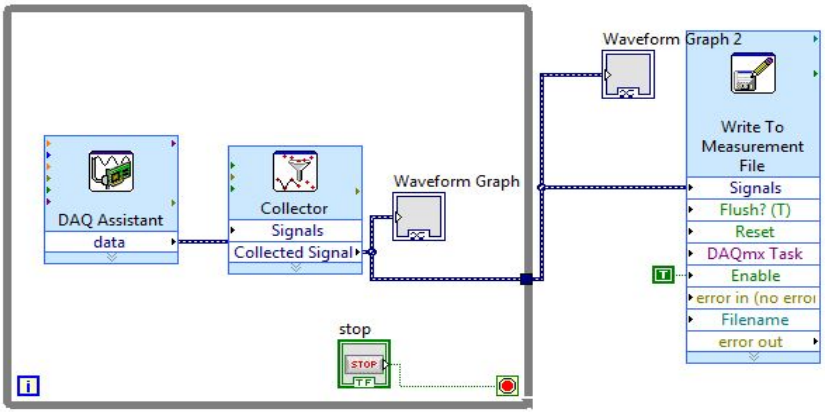

Figure 3.8: Block diagram for the LabVIEW interface for temperature measurement

Two thermocouples placed on top of theupper electrode gas exit, measure the temperature of the gas flow. One thermocouple (Thermocouple 1, indicated with letter 1) at the centre of the top plate and the other thermocouple (Thermocouple 2, indicated with letter 2) at 5 mm distance from centre as shown in the figure 3.10. Thermocouple 1 measures the temperature of the central

jet temperature whereas, thermocouple 2 measures the temperature surrounding the central jet. Temperature measurements were recorded using NI-DAQ temperature input module NI- 9211. A labVIEW program was created to convert the thermocouple output voltage into temperature data points, as shown in figure 3.8. Graphs were plotted for measured temperature with respect to time. The water channel was turned on for all the measurements during the experiments with a flowrate of 10 litres/hour. 100 W transformer was used in the temperature controller. It caused temperature fluctuation in the recorded values with a variation of ±30°C in the heating element due to the power supply used. This difference was very less when the set temperature of the heating element is high. This temperature fluctuation was observed in the measurements as well as on the heating element surface. The reason for this temperature fluctuation was because of the transformer used in the temperature controller. This PID controller provide input power to the heating element based on the temperature in the heating element. When the temperature in the heater exceeds the set temperature, the heater is turned off by cutting down the power supply to the heater. If the temperature is less than the set temperature, the controller provides power to the heating unit to attain the required set temperature. Due to the 100 W power transformer, the minimal power given by the controller increase the temperature by 4°C to 8°C. When the temperature exceeds the required temperature, it turn off the heater causing temperature drop. Moreover, the increased gain of the PID controller particularly at high power supply result in error, causing oscillation in the feedback value to the controller. Thus the power of the transformer was decided to change to 35 W, and the experiments were conducted to check the difference in fluctuation. The maximum temperature reached by the heating element with this power was 306°C. Both the thermocouples placed on the top plate at the exit of the gas flow were at a height of 10 mm from the mica heating element. Figure 3.9 and 3.11 show the temperature profile of the shroud flow gas at different heating element temperature. Temperature at the centre of the top plate is shown in figure 3.9, where the temperature difference was not more than 2°C and the temperature loss is around 50°C at maximum power. This heat loss is minimum when the heating element was at low temperature set points.

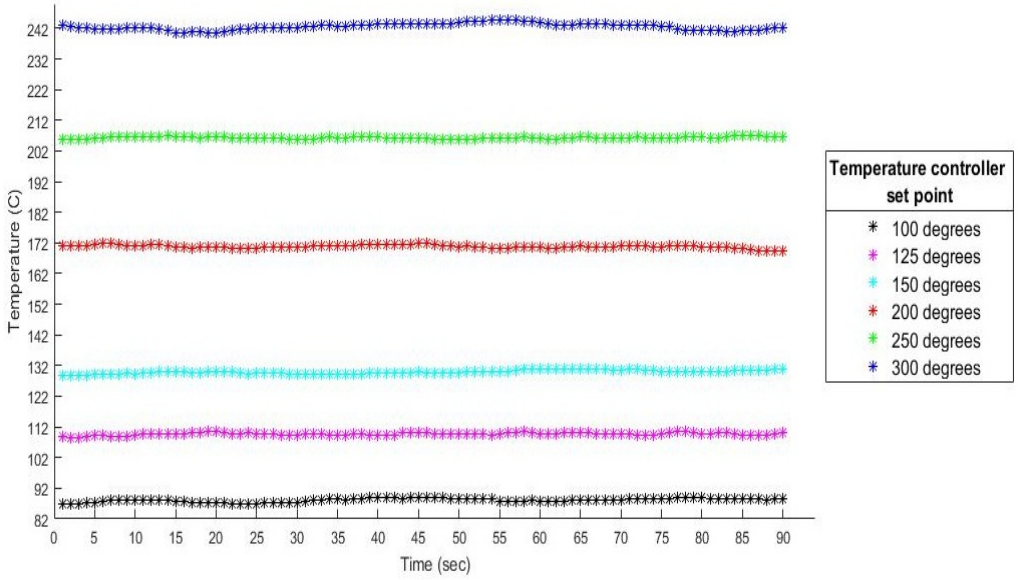

Figure 3.9: Temperature of the preheated shroud flow gas (Thermocouple at the centre of the top plate)

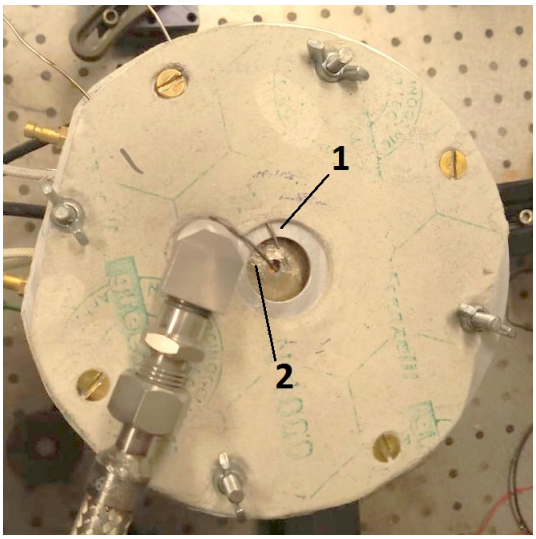

Figure 3.10: Temperature measurement positions of the air flow from the top electrode

The exit diameter of the shroud flow gas is 20 mm. The temperature reduced at every 1 mm from the centre. Figure 3.11 shows the temperature profile of the shroud flow gas at 5 mm distance from the centre of the top plate. The lateral rise temperature was reduced by half when compared to the mica heater temperature. The axisymmetric flow of gas created by the porous ring is the reason for this temperature difference at 5 mm radius from the centre of the top plate. The measured temperature in the 5 mm radius varied constantly around 20°C, whenever the heating element temperature is increased by 50°C.

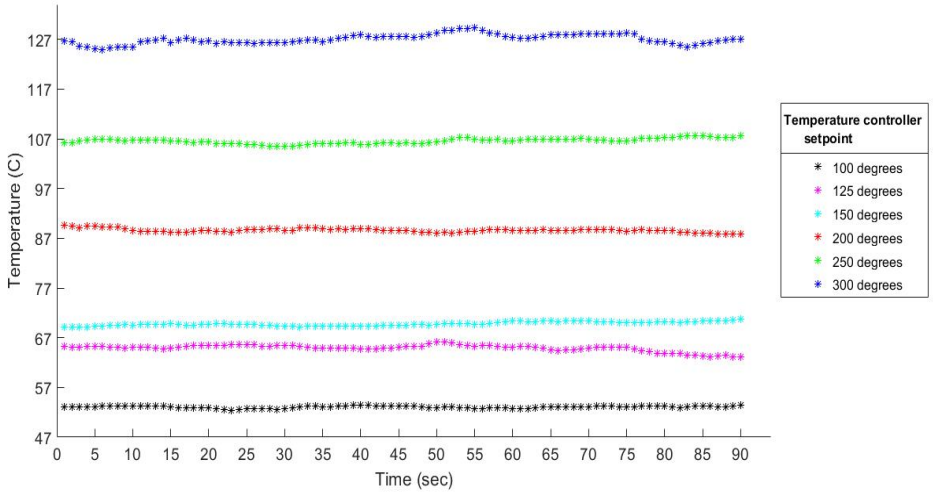

Figure 3.11: Temperature of the preheated shroud flow gas (Thermocouple at 5 mm from the centre of the top plate)

The insulation material inside the aerogel resist up to 600°C, so it was decided to increase the temperature of the heating element up to the maximum limit i.e up to 700°C. Thus, the transformer of the heating element was changed to 50 W, which eventually increased the maximum

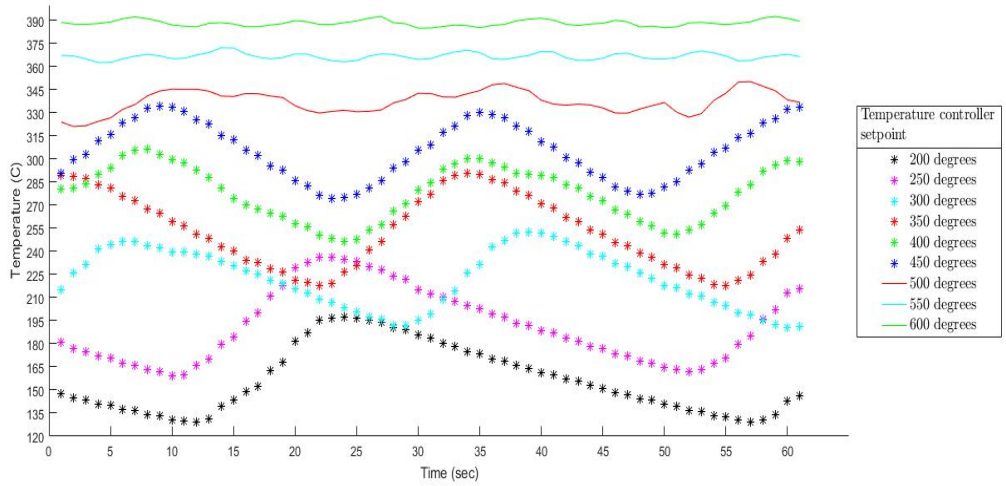

Figure 3.12: Temperature of the preheated shroud flow gas with increased power (50 W) to heating element (Thermocouple at the centre of the top plate)

temperature of the heating element to 685°C. The velocity of shroud flow used during the measurements was 8 cm/s. Temperature measurements at different temperature of the heating element from 200°C to 600°C were carried out. Due to high power supply, the temperature of the mica heating element varied by ±25°C, till 500°C. This fluctuation in the heating element affected the measured temperature profile also. Figure 3.12 shows the measured temperature over time with different heater temperatures. Increase in shroud flow velocity up to 15 cm/s resulted an increase in the measured temperature by 4°C, whereas figure 3.13 represents the temperature profile at a distance of 5 mm from the centre. In this figure 3.13, the temperature fluctuation is low as compared to measured temperature at the centre. But the heat loss was high which eventually gets increased, when the heating element temperature was increased to higher values. Whenever the temperature in the controller was set, measurements were taken after the mica heating element temperature becomes constant or with minimal fluctuation. But in the case of 50 W, the temperature seemed less stable and fluctuations were really high, which could be observed in the feedback of thermocouple in the controller. This caused the greater fluctuation in the measured heat profile (figure 3.12). Moreover, the preheated gas flow was intended to heat zinc metal powders which requires temperature around 600°C to 700°C. Therefore, further investigation of the temperature profile based on the height of the flow was carried out in the presence of central jet along with shroud flow. A quartz tube of the same diameter as the shroud flow exit area was ordered. The quartz tube had a thickness of 3 mm and a height of 10 cm with ten holes of 1 mm, each at 1 cm distance and the tube was placed on the top of the shroud gas flow exit. Temperature profiles based on height for different set point temperatures were measured using a thin thermocouple of 0.33 mm thickness. Temperature for setpoint above 600°C, at various heights above the mica heat element is shown in figure 3.14. When the air gets heated its velocity increases, so the flow rate has to be decreased in order to stabilize the jet. The jet was stabilized at a height of 4 cm from the top plate. Taking that in to consideration, the measurements were recorded up to 4 cm of the jet. From figure 3.14, the temperature fluctuation increased with jet height. It might be due to the heat loss to the surroundings and the fluctuation of power supplied by the controller. Moreover, the previous measurements were only with the preheated shroud flow, but in this case of measurements (figure 3.14), both shroud flow and central jet were used. The central jet is also a considerable cause for heat loss at increased heights. At 1 cm above the heating element, which is a closed area with insulation (from heating element to the top plate surface), the measured temperature values were higher. At other heights, with normal room temperature, the heat

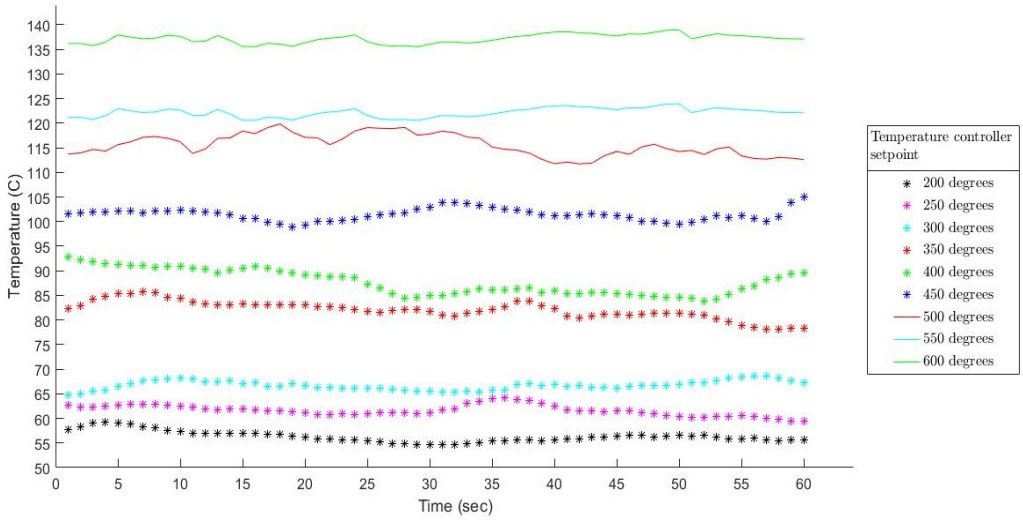

Figure 3.13: Temperature of the preheated shroud flow gas with increased power(50 W) to heating element (Thermocouple at 5 mm from the centre of the top plate)

transfer rate is high. This is the reason for the larger temperature difference between 1 cm and other heights measurement values which is about 100°C as seen in figure 3.14. This temperature difference was really low at heights 2 cm, 3 cm and 4 cm as the heat flow region are mostly of uniform temperature distribution. For other temperatures, the temperature profile is included in the appendix .2.

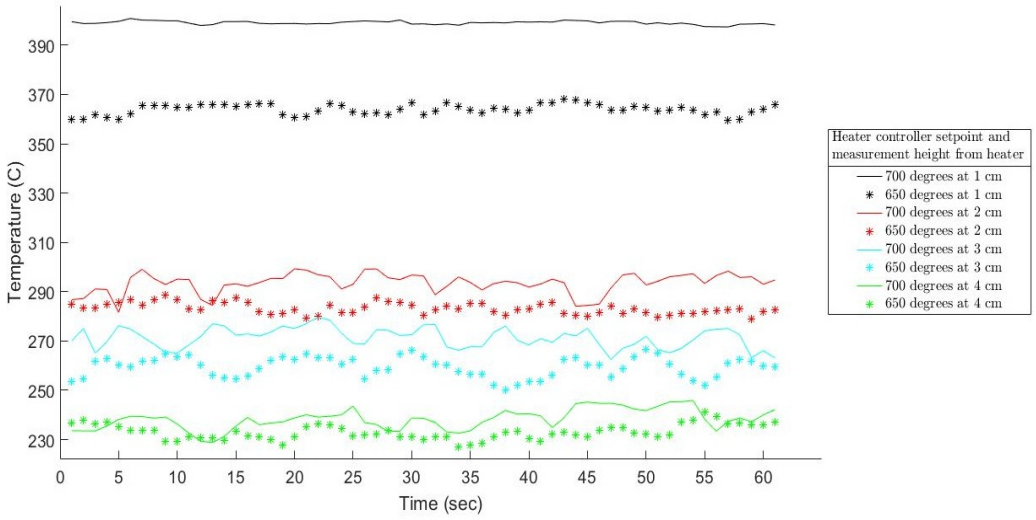

Figure 3.14: Temperature of the preheated gas flow gas (central jet and shroud flow) at different heights (Thermocouple at the centre of the topplate)

Variable voltage controller

The PID controller used for controlling the temperature is not particularly effective, as the power given to the heating element by the controller depends on the transformer. When higher temperature is needed, the transformer ratio has to be changed in the controller. In that case, it is hard to stabilize the temperature of the heating elements at lower temperature set points by

the controller, since the heating element heats up instantly which causes the controller to turn on and off causing the temperature fluctuation. It might be due to the delay in feedback from the thermocouple used. Thus, a variable voltage supply was used as an alternative to the PID controller and the temperature profile fluctuation was verified. The variable voltage controller (PS613) which can provide 0 − 30 V of direct current equipped with an LCD display is used. The current is kept constant and voltage was varied and the temperature for that power in the heating element is recorded. This power supply has the maximum power of 30 W and was the only voltage controller available during the experiments. Voltage and current supplied to the heater were recorded and the temperature achieved with the corresponding power was measured with the thermocouple positioned on the heating element. Another thermocouple was placed at a height of 1 cm from the mica heating element and the temperature around this height was also measured. The temperature profile at heating element and 1 cm from the heating element is shown in figure 3.15. The central jet and shroud flow speeds in the experiments were 100 cm/s and 10 cm/s respectively. The maximum temperature reached by the heating element with 30 W was 307°C. The measured temperature at 1 cm from the heating element in figure 3.15 was almost same as measured data with PID controller with 35 W power (figure 3.9). Moreover, the temperature difference is also large at higher temperatures and decreases when temperature is lowered. Thus, with higher power supply, variable voltage controller has to be used to determine the higher temperature range (around 700°C) which would help in investigating the occurrence of temperature fluctuation when constant voltage is supplied to the heating system. Temperature of the heating element is observed from the display in the PID controller, but in variable voltage controller, it is measured by a thermocouple is recorded using a DAQ interface. Thus, a variable voltage controller with thermocouple feedback and display of input power would be preferred for easier measurement of heating element temperature for respective power supplied. Furthermore, the flow above the top plate is protected by a quartz tube while preheating, if that is insulated the heat loss can be reduced. Another tubular heating system can be placed on the top exit of the plate which is more efficient in heating the gas flow and it should be better for optical access. An idea of winding nichrome wire inside quartz tube and to use as a heating element to preheat the gas flow from the top plate was decided. But due to time limitation, it was not executed. In other case, an inline preheater with low volumetric flow rate can be used and is tightly insulated, particularly the flow connections at the top plate gas inlet. This would help in further optimizing the preheating system for better heat flow measurements at different heights of the jet.

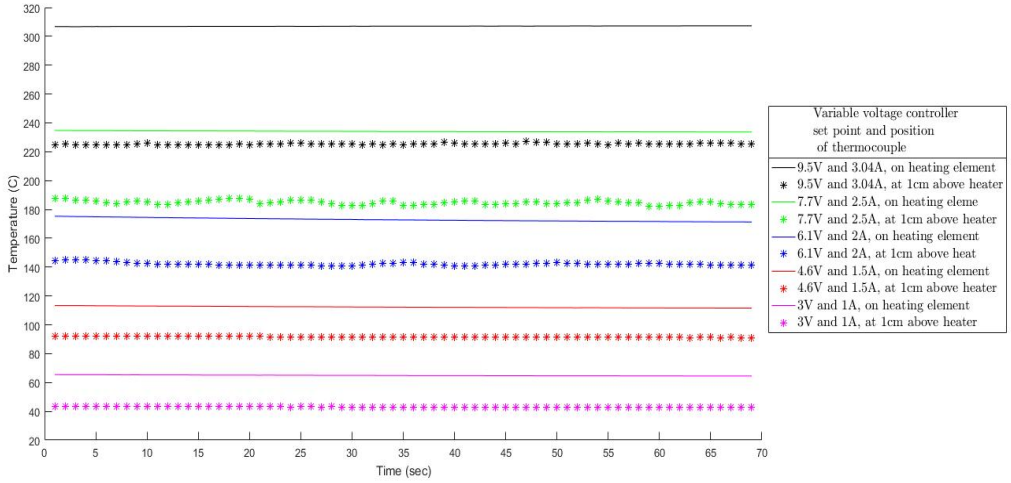

Figure 3.15: Temperature of the preheated gas flow gas (central jet and shroud flow) with variable voltage controller (Thermocouple on the heating element and 1 mm above the topplate)

Chapter 4

Particle Velocity Analysis

For characterisation of flame front and the particle laden jet, optical diagnostics is carried out. The optical setup is installed on the optical table in the laser lab. The burner had two degrees of freedom, vertical and linear adjustment. The vertical adjustment enables the inspection of flame and particle ladent jet at different heights. The horizontal adjustment to move the buner left or right to focus the jet to the camera system. Additionally, lateral adjustment to move the burner front and back is setup. This enables the easier focus of laser sheet on the particle laten jet.

Tracking the particles in the flow during suspension is one of the difficult parameter in particle behavior analysis. As the particle density in the flow is high and flame front diameter required for flame propagation results in optical pathway blocking and there is a significant background noise in the flame front during analysis. several particle interaction mechanism such as friction, mechanical interlocking, inter-particulate forces of cohesion and liquid bridging.

4.1 Photographic device

One of the important devices in optical techniques is the photographic camera to capture images with a short exposure time. These images were later analysed with a PIV analysis tool. A custom made combination of lens and a photographic CCD (charge-coupled device) is used in the setup. JAI TM/RM-2040GE is used to record images of the jet and the flame. It is a progressive scan monochrome camera of 1 inch CCD with a resolution of 1600 $\times$ 1200 pixels and electronic shutter speeds to 1/32,000 sec. In Dual tap mode, the frame rate for a full image is 34 fps. The electronic shutter is controlled by an external trigger using Pulse Width Control mode (PWC). The values given to the external trigger are given in the Appendix .1. The minimum active period of the trigger is 5 μs. The recommend maximum active period can be set less than 1 second but actual maximum period is unlimited. The actual exposure time is equal to the sum of pulsewidth of the external trigger and 7.45 μs. Focused images at different jet heights were taken by mounting several lens to the photographic device. Only two lens yielded good focus. First, the Pentacon (AF) with a minimum focal distance of 50 mm and diaphragam of f/1.8 which has M42 mount, so it is connected to a c-mount adaptor to fit to the camera. Another lens used is Navitar Zoom 6000 lens of unknown specification. The observed minimum focal distance for this lens during experiments is 35 mm. This lens has a higher magnification with less distortion, which was helpful in tracing the particle during PIV analysis. Therefore, this lens is used to focus the jet in more detail with an area of 6mm $\times$ 6mm. Figure 4.1 shows two pictures of burning iron with flame front, one with the Pentacon lens and one with the Navitar lens.

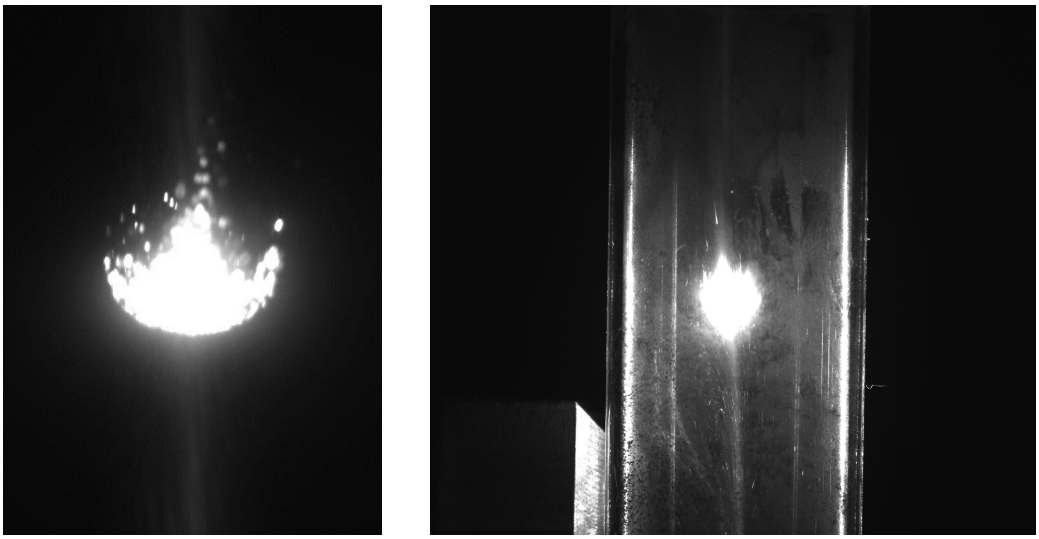

(a) Pentacon lens (b) Navitar lens

Figure 4.1: Flame images of carbonyl-iron powder burning in air

4.2 PTV analysis

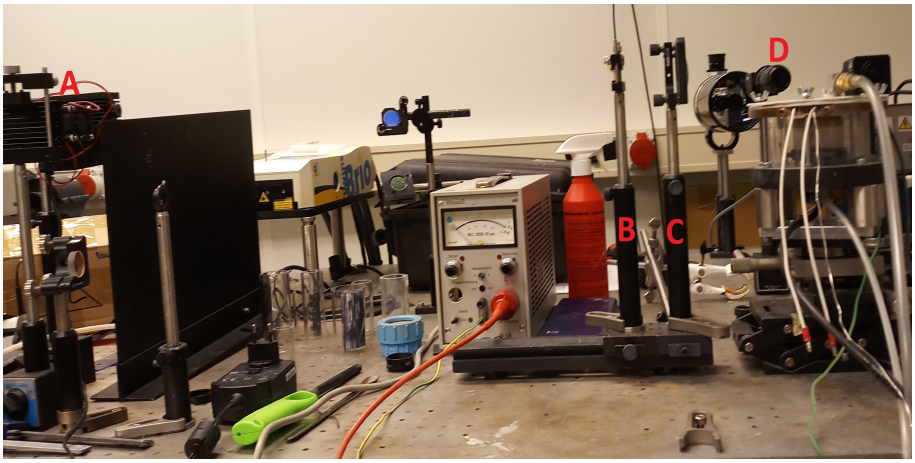

Figure 4.2: Experimental setup with devices labelled with letter

PIV analysis involves tracing the displacement of group of particles in the fluid flow. A PIV setup consists of a laser, tracer particles in the flow and a photographic device with focussing lens. The experiments were planned to be carried out using dual pulsed Quantel Twins-BRIO Nd:YAG laser. Using the double pulse, consecutive images of the particles in the flow are taken. With these images cross correlation is performed to find the velocity of the particles. The period of illumination should be very short, so that the particle in the flow is imaged instead of particle streak. Due to some technical problems in the double pulse laser, a DIY blue laser with a wavelength of 450 nm and a power of 5.5 W was used. The total setup for the PTV analysis is shown in figure 4.2. This laser (labelled as A in the figure 4.2) creates a continuous laser beam which could be modulated using DG1000 Arbitrary Waveform Function Generator. Due to the high power of the laser, the duty cycle of the laser beam has to be reduced to 5% using the TTL waveform generator. A laser sheet with very accurate focussing is created by using convex and concave lens (indicated by letters B and C). The JAI camera (indicated as D) is used as photographic device which allows

triggering based on different modes. A Stanford Research Systems DG535 trigger box is used to control the exposure time of the camera. The images are recorded using the photographic device with a region of interest by adjusting the focus of the lens. The lens is focussed on the jet flow and the real dimension of the focussed region is recorded using a scale post. When the real dimensions of the focussed region and the frequency of the pulses are known, the velocity of the particle can be calculated using particle displacement. The frequency of the laser used for the analysis is 1000 Hz, from this the time period can be calculated. The exposure time of the camera is controlled by the trigger box using JAI SDK program. The region of interest (ROI) is approximately 6 $mm \times 15$ mm high. The images are analysed in PIV View where auto-correlation method is used to evaluate the image. Region of interest is selected and the correlation windows size is Based on the particle streaks in a single image, the displacement of particle is obtained from which velocity can be determined. From figure 4.3, the displacement of the particles which is about 300 μm and the time period calculated from the frequency is 10^{-3} s, gives the velocity of the particle at the exit of the top plate is around 0.3 m/s. The particle is traced about 8 times in the image. Subsequently, velocity of the particles in the middle region of the jet is determined using Navitar lens of 6 mm region of interest. It is shown in figure 4.4. The velocity of the particle at the centre decreases from 0.16 m/s to 0.12 m/s approaching the region of stable aerosol cloud. Figure 4.5 shows further 6 mm height of the jet near to the flame zone where the density of the metal particles is higher and the particle velocity reached is 0.1 m/s. Due to the flame, the velocity near the flame zone during combustion was very hard to determine. A neutral density filter of 450 nm is used along with the camera to capture the jet region below the flame zone. But the images obtained did not result in evaluating the velocity of the particle near that flame region. The velocity of the iron particles is less than half of the velcoity of the air flow. It has the maximum velocity of 0.32 m/s to the minimum velocity of 0.1 m/s. As the density of the particles above the velocity of 0.1 m/s is high, tracking the particles above this is hard and did not yield better results. Moreover the particles entrained in the flow increase in diameter eventually from the exit of the top plate which was shielded by the shroud flow. However, some particles were lost from the flow during dispersion.

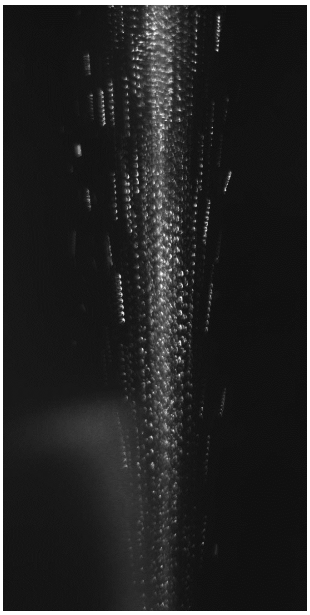

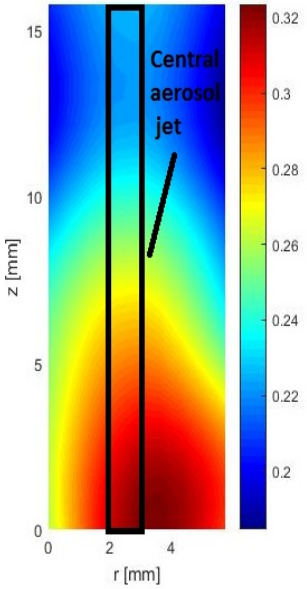

(a) PTV image of the iron aerosol jet near to the stagnation of aerosol cloud where flame occurs
(b) Velocity contour with the central aerosol jet of 1 mm

Figure 4.3: PTV image evaluation by PIV View using Pentacon lens for a jet height of 1.5 cm with an exposure time of 12 ms

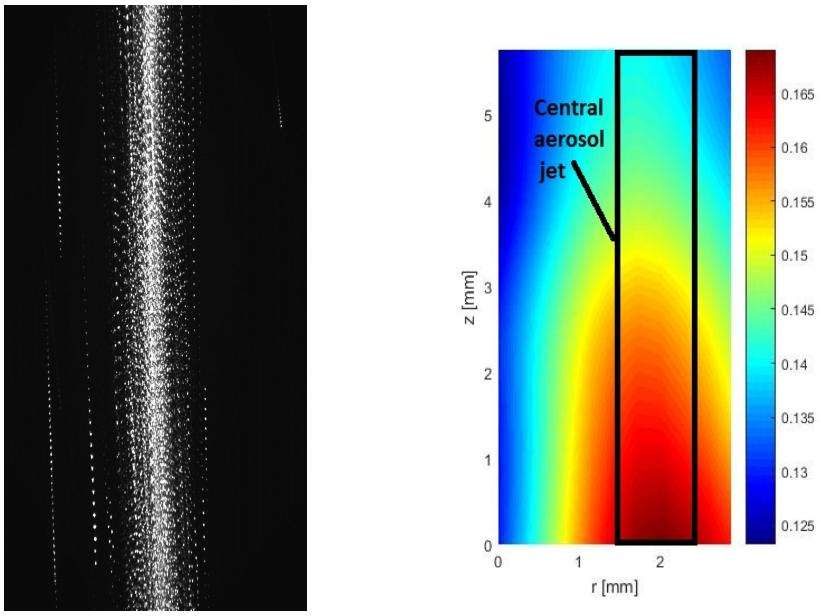

(a) PTV image of the iron aerosol jet with a region of interest of 6 mm (b) Velocity profile of the particles in the jet

Figure 4.4: PTV image evaluation by PIV View using Naviator lens for a jet height of 6 mm with an exposure time of 22 ms

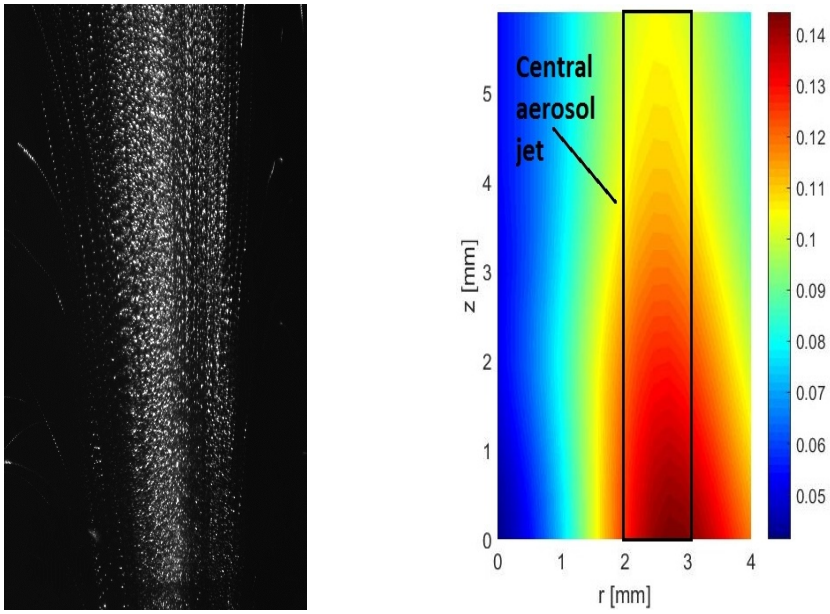

(a) PTV image of the iron aerosol jet near to the stagnation of aerosol cloud where flame occurs (b) Velocity contour of the particles in the jet with highest velocity (0.14 m/s) of the particle to the lowest velocity (0.1 m/s)

Figure 4.5: PTV image evaluation by PIV View using Navitar lens for a jet height of 6 mm with an exposure time of 22 ms

Chapter 5

Number Density

This chapter involves the estimation of number density of iron particles in the metal-air aerosol flow. First, the importance of estimating number density of the metal aerosol is explained. Second the flow behavior of metal aerosol and the experimental approach to capture the metal particles is detailed. The final section includes the results obtained and the inferences are discussed.

5.1 Number density estimation

Number density of aerosol is the measure of number of particles in the flow based on the aerosol density. Number density is one of the parameter in metal aerosol characterization. Based on the amount of unburnt particles after combustion ranging from more than 90% to less than 1%, the characteristics of the combustion process can be known. The combusted metal particles were captured in order to estimate the number density of metal particles discharged in the flow during dispersion. A procedure is developed for measuring the number density of spherical particles having diameters 5 to 9 μm by a simple experimental approach. This procedure is developed based on characteristics of the metal dust burner designed to produce a self-sustaining aerosol flame. Since the burner is designed based on flow independent particle density control, by adjusting the voltage, the density of the particles in the flow can be controlled. But it is important to know the concentration of particles in the flow to optimize the burner to use the metal fuel at its full potential. The principle of determining the particle concentration relies on two measured quantities, namely, the mass and volume of the sample. In this burner setup, the aerosol particle density depends on the mass flowrate and the volumetric flow rate of the aerosol. This approach is focused to measure the mass flow rate of the aerosol in the flow. This is done by capturing the metal particles from the aerosol flame. A definite concentration of particle is required in the flow for a stable flame which is the reason for capturing the particles during flame. Before capturing the particles, dynamic behavior of aerosol during dispersion needs to be known. Terminal settling velocity is one of an important parameter to be considered in this case, as explained in the following section.

5.2 Terminal settling velocity

In many practical problems, the resistance caused by air molecule layers is either small or is not important, and therefore can be ignored [50]. The metal particles in the air flow forms a stable cloud where the combustion zone occurs. At this point, particle moving in the fluid reduces to almost zero and there occurs the phase separability of fluid and particles. The forces acting on the particles are gravity and drag. The drag force is the resistance force caused by the motion of the particle through the fluid. It is directly proportional to the velocity of the particle in the fluid flow. At a point, the drag force becomes equal to the gravitational force, this is called terminal velocity of the particle. This can be seen in the Figure 5.1.

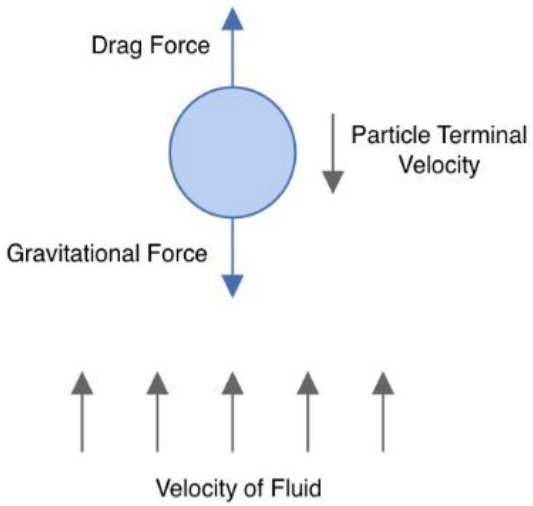

Figure 5.1: Terminal settling velocity of the particle in fluid flow

The density of the particle at the exit of the top plate increases over the height of the aerosol jet. When the density of the particle cloud becomes higher than the fluid density, the particle starts to settle which on ignition occurs the stable flame front as shown in figure 5.2. The settling velocity of the particles must be greater than the fluid velocity in this case. when the particle is carried over in the flow, the settling velocity is less or equal to the bulk fluid velocity. Moreover, the amount of particles entrained are less than the fluid volume for entraining. The metal particles are 5 to 9 μm and spherical in shape. The fluid flow regime is laminar, it is determined by using the following equation 5.1.

$$Re = \frac{\rho_f V D_p}{\mu} \tag{5.1}$$

$$V_t = \frac{(\rho_p - \rho_g) g D_p^2}{18\mu} \tag{5.2}$$

The iron particle used is 44890 ALDRICH where the size, purity, and density was given in the data sheet. In equation 5.1 and 5.2, D_p is the diameter of the particle which is in the range of 5 to 9 μm (average of 7 μm is taken as D_p), g = 9.81m/s^2 is the acceleration due to gravity, Re is the Reynolds number, V is the velocity of the fluid (air), V_t is the terminal settling velocity of the iron particle, μ is the viscosity of the fluid (air), ρ_f is the density of the particle, ρ_p is the density of the fluid. Dynamic visocity of air at room temperature is $\mu = 1.81 \cdot 10^{-5}\ kg/ms$. Density of air at room temperature is ρ_f= 1.2260 kg/m^3. Velocity of air used in the experiment is 1 m/s, which is the velocity of the central jet (at this velocity, the jet is stable). Thus, by substituting the values in 5.1, Re is equal to 0.48, which corresponds to laminar flow. When Re < 2, the terminal settling velocity of the particle can be found by substituting the values in equation 5.2. From the data sheet of the iron powder, the density of the iron particle at room temperature (ρ_p) is 7860 kg/m^3. Substituting the values in equation 5.2, the terminal settling velocity of the particle (V_t) is 0.035 m/s. At this velocity, the particle starts to settle down and flame front occurs at this point on ignition.

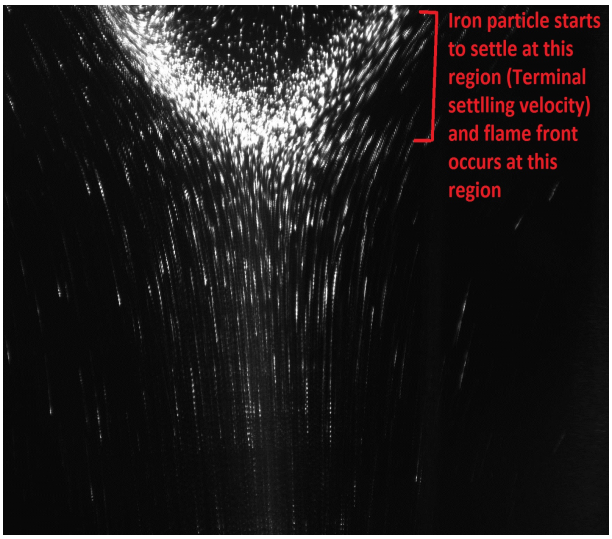

Figure 5.2: Stable zone of the aerosol cloud where ignition occurs. Image taken using Naviator lens during iron aerosol dispersion using M^{2}DB

5.3 Experimental approach

For capturing the combusted metal particles, the filtration system was designed and assembled, it includes a Sterlitech PPO 47 filter holder and PVDF membrane filter of 0.1 μm pores. The metal particles are captured and held by the filter using suction pressure provided by a vacuum cleaner. This capturing is done for a defined time. The mass before and after capture of metal particles by the membrane filter is weighed. Thus, the mass flow rate of the aerosol is found from the mass increase for a measured time. From the mass flow rate, the aerosol mass density and the average number density was calculated. Figure 5.3 is the experimental setup with filter element to capture the particles. As the particle jet flow exits through 1 mm diameter of the top plate, the area of the particle jet increases over the height of the jet where the velocity of the flow is considered in the estimation of number density. When capturing the particles using the filter elements there is no particle loss observed for the specified time duration.

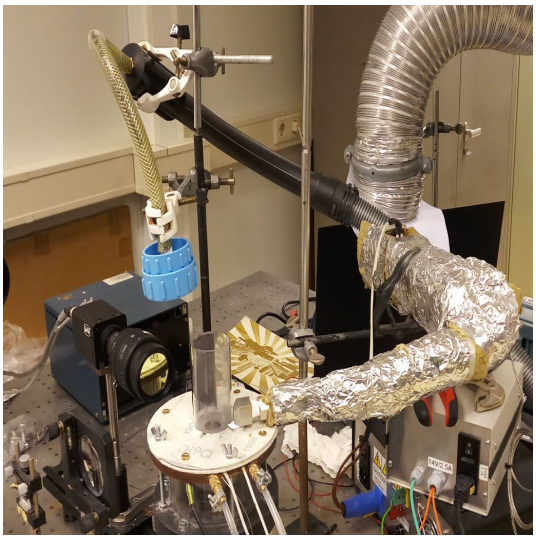

Figure 5.3: Experimental setup for capturing the metal particles

The parts involved in the filter element assembly and membrane filter are shown in figure 5.4. The filter has an open face where the membrane filter can be placed between polypropylene support screen (4) and Base O-ring FPM (2a). A small silicone O-ring is attached to the support screen (1). The membrane filter was placed over the polypropylene support screen (4) and closed by Polypropylene locking ring (1). Suction happens in the surface of outlest base (6) and the vacuum hose is connected to the outlet adapter (7). Initially the suction is not enough to hold the particles, when the membrane filter placed over the support screen. Later it was found that because of the smaller pores (0.1 μm), low suction pressure is created between the memebrane and the support screen. Inorder to have suction pressure to hold the particles, the membrane filter was placed between the locking ring and the O ring. This created a pressure build up between the filter and screen which holds the particles on the filter.

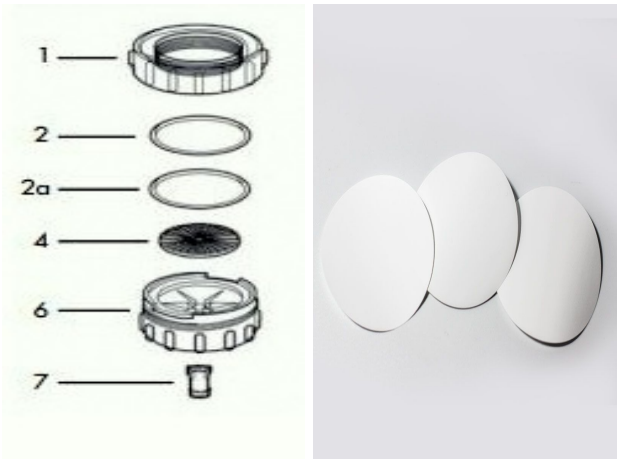

Figure 5.4: Filter holder parts (left) and PVDF membrane disc(right)

Due to the pressure between the membrane filter and polypropylene support screen, the membrane filter tends to slip while capturing the particles are collected towards the edge of the filter which leads to particle accumulation and particle loss (they stick to the filter O ring and collected over the corner as can be seen in figure 5.5). Another base O ring of same diameter was mounted above the support screen. Thus, the membrane filter is now placed between two base O-rings and tightened with the locking ring. Since the pressure between the membrane and the support screen is high, membrane filter tears off, when the vacuum cleaner suction is increased or filter assembly is connected to the vacuum cleaner under pressure for long time. Therefore, the filter element with membrane is only connected at the time of time of capturing or else dismounted from the vacuum hose. After several trials, the polypropylene support screen of the filter is affected with combusted fumes of iron oxide. It is due to the heat of iron oxide fumes. This was avoided by increasing the distance between the combustion zone and the filter element.

After repeated trails it was decided to capture the particles for 30 seconds. Initially, the time duration for particle capture was 60 seconds. The membrane filter has pores of 0.1 μm, where the particles stick to the membrane as there is a suction developed over the surface. For a longer duration, the particles settling concentration over the membrane is high which leads to fall of few particles as the particles block the pores when captured. Moreover, the flame sometimes blows out when the particle density is low. Figure 5.6 shows the capturing of combusted iron particles by the filter element with membrane filter. Repeated trials were done for a specific voltage of 5 kV with central jet velocity of 100 cm/s and shroud flow velocity of 6 cm/s. The initial weight of the membrane filter is 0.1028 g. After 8 trials, due to reduced density of the particles, the aerosol jet does not have a stable flame. Figure 5.7 shows the membrane filter with captured iron products after combustion. Table 5.1 shows the number density estimation, calculated from the final weight

Figure 5.5: Particles collected over the edge of the membrane filter

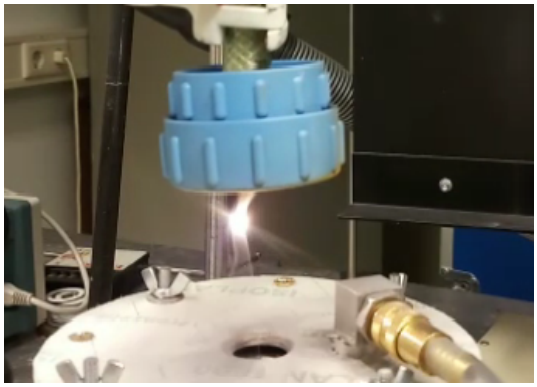

Figure 5.6: Combusted iron particle collection using filter

of the captured combusted particles in the membrane filter. A certain concentration of particles is needed for a stable flame, if it reaches the lower limit, the concentration has to be increased by increasing the voltage potential. Figure 5.8 shows the plotted results obtained from the captured combusted particles over time period of 240 seconds. The number density of iron particle decreases at an unpredictable scale as seen in table 5.1 due to the varied density of charged particles between the electrodes. Thus for comparison, the test was carried out to capture non-combusted iron particles and combusted iron particles. Table 5.2 represents the number density estimation of non-combusted and combusted iron particles captured by successive trials. From this table, the number density of the particles reduces approximately around 20% for every trials for both non-combusted and combusted iron particles.

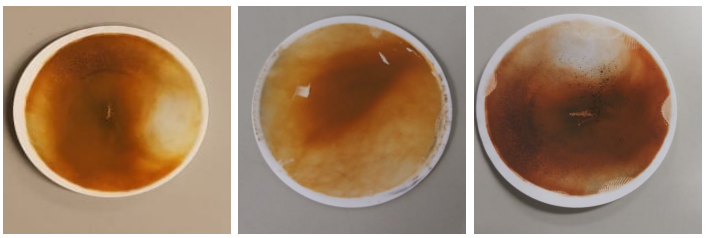

Figure 5.7: Combusted iron products captured in the membrane filter(grey oxides are magnetite and yellow or reddish brown oxides are hematite)

The captured oxides indicated presence of two types of oxides. Figure 5.7 shows the presence of Fe_3O_4 (magnetite, grey in color) and Fe_2O_3 (hematite, yellow or reddish brown in color). Occur-

Table 5.1: Number Density estimation from mass of captured particles

Trial	**Time**	**Initial weight**	**Final weight**	**Mass flowrate**	**Volumetric Flow rate**	**Aerosol density**	**Mass of particle**	**Number density**
	(sec)	**(g)**	**(g)**	10^{-3} **g/s**	cm^3/s	10^{-3} **g**/cm^3	10^{-9}**g**	10^6 **1**/cm^3
Trial 1	**30**	**0.1028**	**0.1376**	*1.20*	*0.785*	*1.50*	*1.411*	*1.05*
Trial 2	**30**	**0.1028**	**0.1364**	*1.10*	*0.785*	*1.40*	*1.411*	*1.01*
Trial 3	**30**	**0.1028**	**0.131**	*0.94*	*0.785*	*1.20*	*1.411*	*0.85*
Trial 4	**30**	**0.1028**	**0.1295**	*0.89*	*0.785*	*1.10*	*1.411*	*0.80*
Trial 5	**30**	**0.1028**	**0.1252**	*0.75*	*0.785*	*0.95*	*1.411*	*0.67*
Trial 6	**30**	**0.1028**	**0.1204**	*0.75*	*0.785*	*0.75*	*1.411*	*0.53*
Trial 7	**30**	**0.1028**	**0.1196**	*0.56*	*0.785*	*0.71*	*1.411*	*0.51*
Trial 8	**30**	**0.1028**	**0.1174**	*0.49*	*0.785*	*0.62*	*1.411*	*0.44*

Table 5.2: Number density estimation of iron particles with and without combustion

Trial	**Time**	**Initial weight**	**Final weight**	**Mass flow rate** 10^{-4}	**Volumetric Flow rate**	**Aerosol density** 10^{-4}	**Mass of particle**	**Number density** 10^5
	(sec)	**(g)**	**(g)**	**g/s**	cm^3/s	**g**/cm^3	10^{-9}**g**	**1**/cm^3
Without combustion								
Trial 1	*30*	*0.1028*	*0.1132*	*3.47*	*0.785*	*4.42*	*0.709*	*6.23*
Trial 2	*30*	*0.1028*	*0.1104*	*2.53*	*0.785*	*3.23*	*0.7109*	*4.55*
With combustion								
Trial 3	*30*	*0.1028*	*0.1226*	*6.60*	*0.785*	*8.41*	*1.4109*	*5.96*
Trial 4	*30*	*0.1028*	*0.1194*	*5.53*	*0.785*	*7.05*	*1.4109*	*5.00*

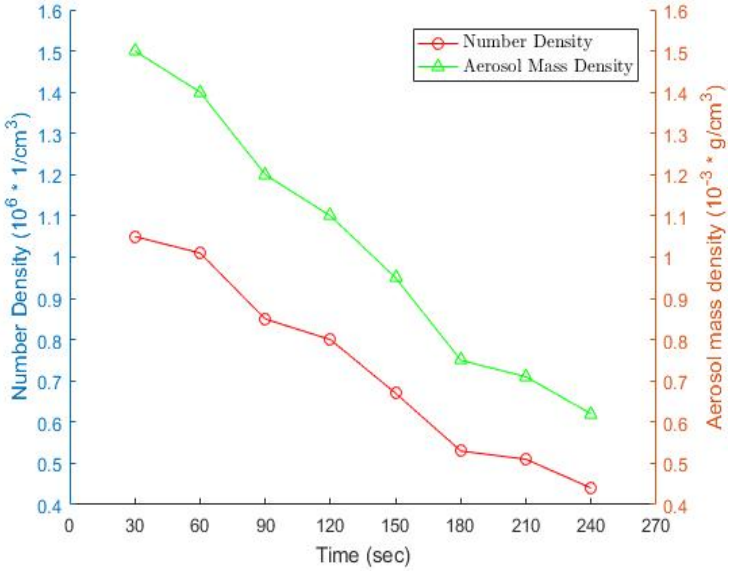

Figure 5.8: Number density and Mass aerosol density profile over time period

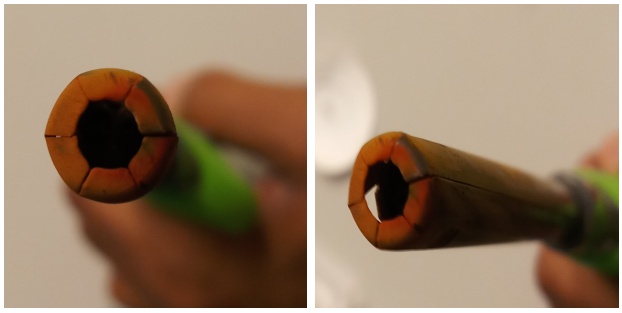

Figure 5.9: Red iron oxides (Hematite) near the iron flame front

rence of hematite after combustion was higher when the oxygen concentration was increased. As hematite is formed in different colors, when oxygen concentration was increased over 60%, red iron oxides (Hematite) were formed which is prominantly seen only near the iron flame front. Thus, it was hard to capture those red oxides near the flame zone. Some deposits were found on the gas lighter during ignition of the flame as can be seen in figure 5.9. The amount of magnetite present during the experiments are really low. When the powder in the capacitor is reloaded with iron powders from the storage container, then the collected iron oxides show presence of magnetite. If the experiments were continued with the same powders left on the capacitor for the following day, magnetite was hardly seen in the combusted products. It is due to the oxidation of iron powder with the air in the dispersion chamber. Additionally, the grey oxides (magnetite) seemed much larger in size than hematite. Therefore, further investigation of the captured iron oxide was carried out to find the diameter of the products formed.

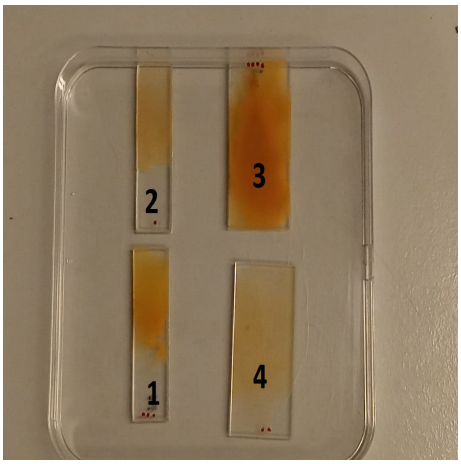

Figure 5.10: Iron oxide samples in the petridish for microscopic analysis with number indicated for two different oxygen concentration and height

5.4 Optical size determination

Initially, the captured iron oxides were analyzed using optical microscope in the Multiscale lab at the university. The central jet and shroud flow velocity used for collecting samples are 100 cm/s and 7 cm/s. Four glass pieces with area of 4 cm^2 and 8 cm^2 were used to collect the specimens (iron oxides). The glass surface is uniform and clean where the iron oxides were collected and stored in a petridish to prevent deposition of impurities on the sample. The samples were collected on two different oxygen concentration (21% and 60%) and at different heights (near the flame zone and at a height of 10 cm from the flame zone). As shown in figure 5.10, sample 1 and 2 were collected near the flame and at a height of 10 cm at 21% oxygen concentration. Sample 3 and 4 were collected near the flame and at a height of 10 cm at 60% oxygen concentration. The combusted iron loses heat and increases in diameter after combustion. Thus, it was decided to capture the iron oxide near and at a distance from flame zone to analyze the diameter of the iron oxide formed. The sample is analyzed in optical and scanning electron microscopes. Figure 5.11 shows the optical microscopic images of iron oxides captured near the flame zone with 21% oxygen concentration. As the products are captured near the flame zone, most of the products in the sample are less than 6 μm which is focussed in the figure 5.11(b) and the larger particles in the figure 5.11(a) are around 28 μm to 38 μm. When iron particles inspected under optical microscopy, the light beam which incident on the particle surface directly perpendicular to it which makes the particles to appear like hollow structures during imaging which is observed in all optical microscopy images. In figure 5.12(b), the diameter of the combusted iron particles are in the range of 20 μm to 30 μm which represents that diameter of the particle tends to increase after some height, although there is a presence of smaller particles with size of less than 5 μm as seen in the figure 5.12(a). Particles are almost found separately with no agglomeration or any structures at 21% oxygen concentration.

With 60% of oxygen concentration, the sample collected near the flame has particle sizes between 5 μm to 6 μm as can be seen in the figure 5.13(b) and the maximum diameter of the particles present in the sample are around 10 μm as inferred from fig:60near(a). Few particles were agglomerated at higher oxygen concentration as the amount of oxygen makes the flame brighter and the heat released is higher. Due to the increased heat, these oxide size were found no larger than 10 μm. The sample collected at a height of 10 cm has also the same maximum diameter and the particles settled together as seen in the figure 5.14(a). Due to higher oxygen concentration, the flame temperature during combustion increases which might caused a sintering effect between the particles which is the reason for particle agglomeration after combustion. The sample is further analyzed in scanning electron microscope for clear structure and diameter of the particle. Due to

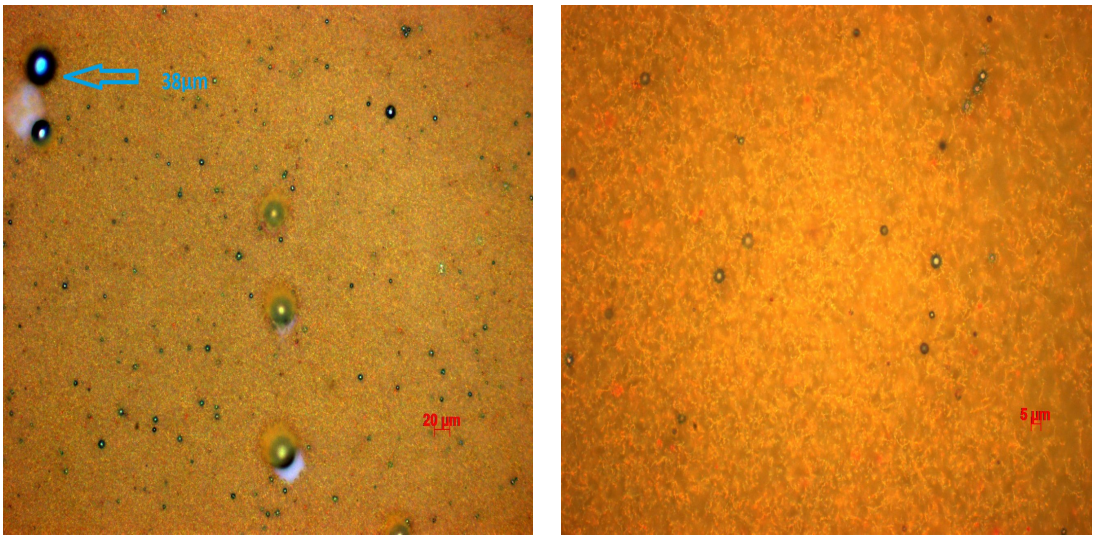

(a) Large sized iron oxides of size 28 to 38 μm (b) Magnified view focussing the iron particle of size 5 μm

Figure 5.11: Optical microscopy images of sample collected near flame zone (21 % oxygen)

the use of glass as base plate for specimen, clear images of the sample was not achieved in SEM. Due to time constraint, further specimen analysis with a copper base plate was not carried out. Figure 5.15 shows the SEM images of combusted iron powder. Particle agglomeration is seen in the figure 5.15(a) and the particle size in the range of 20 μm to 40 μm as represented previously in figure 5.12. The combusted products collected near the flame zone at 60% oxygen are in the range of 5 μm to 10 μm as inferred from the figure 5.15(b). In 60% oxygen concentration, oxides formed were mostly in nanometers. However, clear results were not inferred during the tests. The samples are collected in a quenched copper plates for less than a couple of seconds and also for a longer duration of 60 seconds, helps in investigating the structure of the iron oxides in more detail and understanding the morphology of the products formed. It would be interesting to see the shell structure and oxide diffusion on iron particle surface as iron is one of the metal which undergo two kinds of combustion mode during heteregenous combustion. Formation of gaseous oxides and sub-oxides which are in nanometers formed during high oxygen concentration. In other case, formation of porous oxide shell resulting in size of micrometers which occurs in air or at low oxygen concentration.

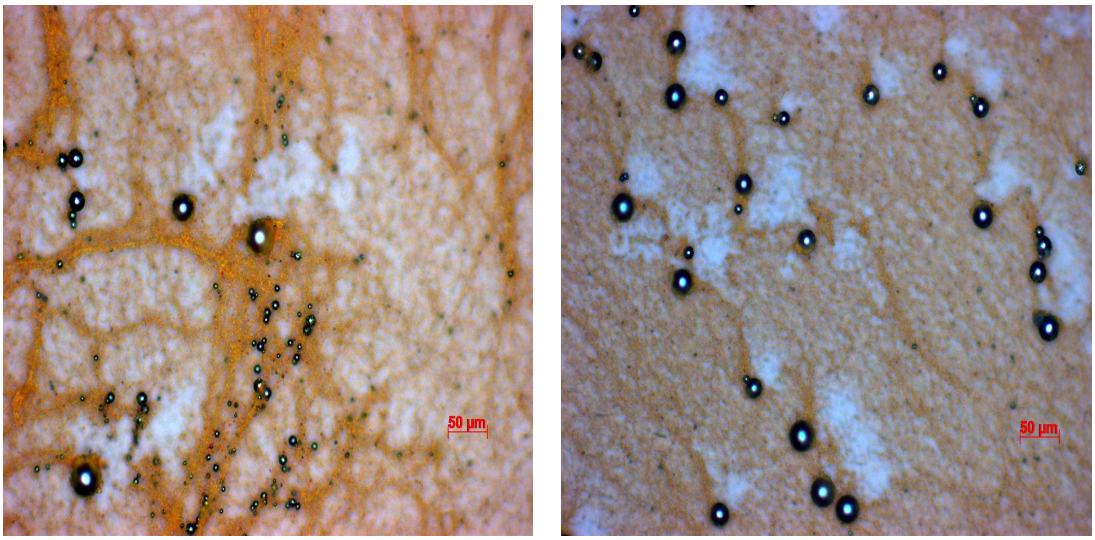

(a) Particles less than 7 μm are present along with some large particles size of 40 μm (b) Magnified view focussing the iron particle of size between 20 to 40 μm

Figure 5.12: Optical microscopy images of sample collected at a height of 10 *cm* from flame zone (21 % oxygen)

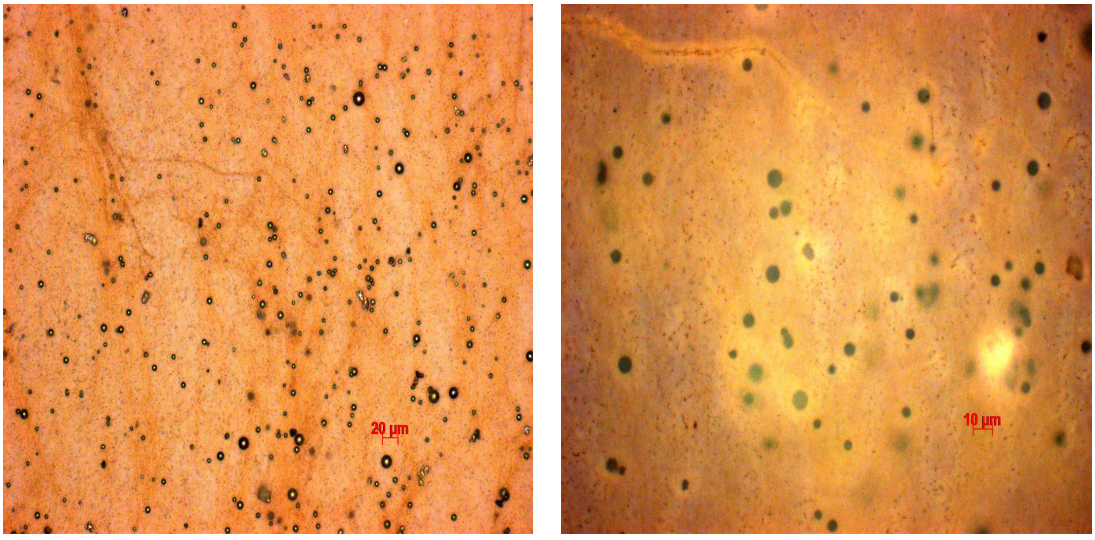

(a) Particles less than 7 μm are present along with some large particles size of 10 μm (b) Magnified view focussing the iron particle of size less than 10 μm

Figure 5.13: Optical microscopy images of sample collected near flame zone (60 % oxygen)

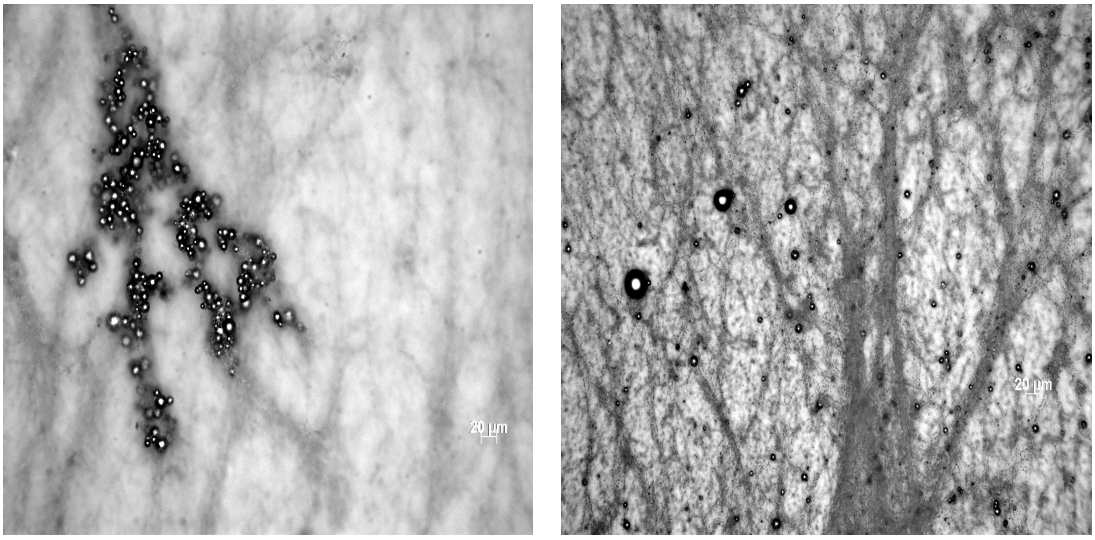

(a) Zoom out image of a section of sample (b) Magnified view focussing the iron particle of size between 4 to 10 μm

Figure 5.14: Optical microscopy images of sample collected at a height of 10 cm from flame zone (60 % oxygen)

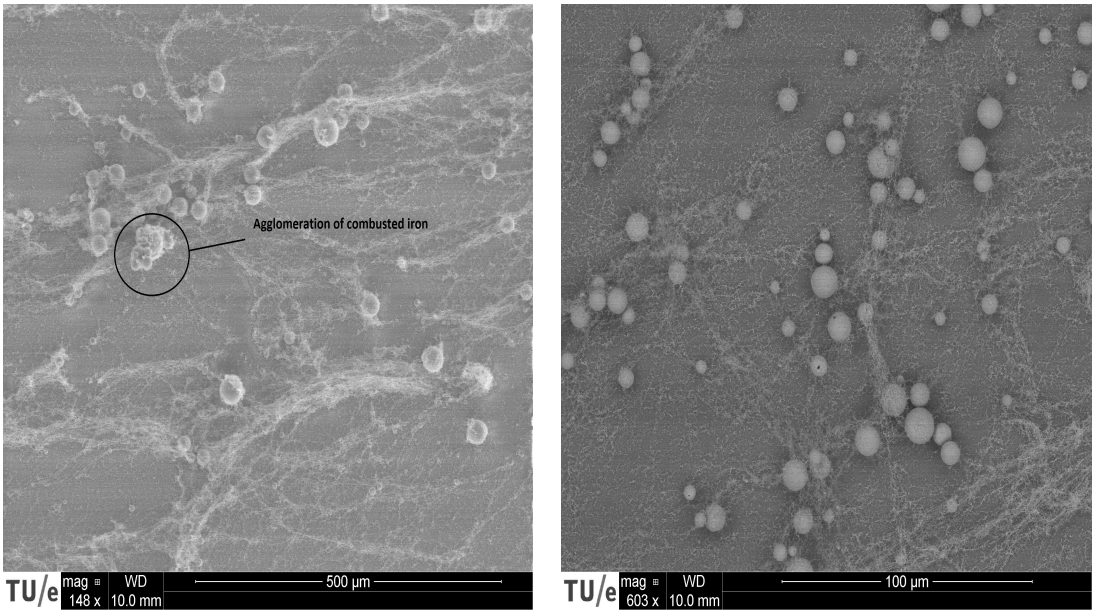

(a) Image of sample at 10 cm from the flame zone (21% oxygen) (b) Image of sample near the flame zone (60% oxygen)

Figure 5.15: SEM images for sample of combusted iron powder

Chapter 6

Investigation of Zinc Metallic Aerosol

This chapter discusses the flammability of zinc aerosol with and without preheating in the M^2DB setup. Several tests were carried out at different oxygen concentration and temperature. These tests were done to understand the flammability of zinc cloud and to optimize the burner in the aspect of creating a stable flame front.

6.1 Combustability of Zinc aerosol

Iron aerosol yielded a stable flame in the M^2DB setup and the characteristics of the flame is discussed in the previous chapters. Subsequently, experiments were carried out to burn zinc aerosol in the burner system. As zinc is a highly volatile metal, the combustability of zinc is very interesting to investigate. In air, zinc reacts with oxygen to form zinc oxide with a white or bluish flame. Due to zinc's low melting point of 419°C, zinc dust clouds react with pure oxygen at 149°C and ignition occurs at 500°C) with a bluish flame. In air, zinc dust clouds ignite at 600°C [51]. The zinc powders used for the experiments are given in the Table 6.1.

Table 6.1: Zinc powders used for experiments

ID	Specie	Purity [%]	Particle size [μm]	Info
Zn-1	Zn	≥ 98	< 10	209988 Aldrich
Zn-2	Zn	-	-	96454 Aldrich

6.1.1 Flammability test in preheated burner system

As inferred from the literature review, the combustion of zinc requires higher temperature. Thus, experiments were first carried out in the micro metal burner with preheating system. This burner system creates a stable aerosol jet when the central jet and shroud flow velocity are 100 cm/s and 7 cm/s respectively. The temperature of the heating element is maintained at 685°C. This is the maximum temperature that can be achieved by the heating system, which is limited by the insulation material used in the heating system. The temperature of the aerosol jet at the exit of the top plate reaches 400 $°C$. The temperature profile and heating system information can be found in section .2 . First, Zn-2 powder was used in the combustability test. The voltage supplied was varied between 2.5 to almost 5 kV to increase the particle concentration in the flow to achieve a flame zone during ignition. But the aerosol jet was unsteady and the zinc aerosol burned only in the presence of gas lighter. During preheating, the density of the air decreases

which created instability of the aerosol jet. Decreasing central jet velocity to 75 cm/s and the shroud flow velocity to 5 cm/s has a considerable effect resulting in aerosol instability. Moreover, reduced gas flow velocity tends to have increased temperature at the aerosol jet cloud with an eventual decrease in jet height. From figure 3.14, the temperature of the gas flow at a jet height of 4 cm is around 240°C, which is sufficient for zinc dust clouds ignition with pure oxygen [51]. The oxygen concentration in the shroud flow remained 100 % for all the experiments for increased reactivity of zinc with oxygen. In the central jet, the oxygen concentration in the air flow was varied from 40 to 100 %. Until the oxygen concentration was set to 80 %, the zinc aerosol burns only with the presence of gas lighter. On reaching 100 % oxygen concentration in the central jet, the aerosol started to acquire flame with the gas lighter. After several attempts, the jet cloud ignited with a bright flame and the zinc is combusted. But the occured flame at the zinc cloud started to propagate towards the aerosol exit resulting in flashback. Immediately, the voltage and the air flow were cut down as the oxygen concentration is 100 % inside the dispersion chamber.

(a) Mica Heating element and aerogel burnt by zinc flame

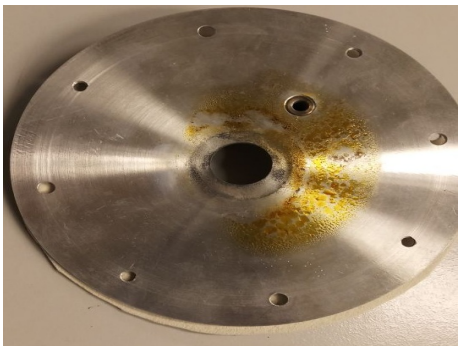

(b) Aluminium top plate with deposits of zinc oxide

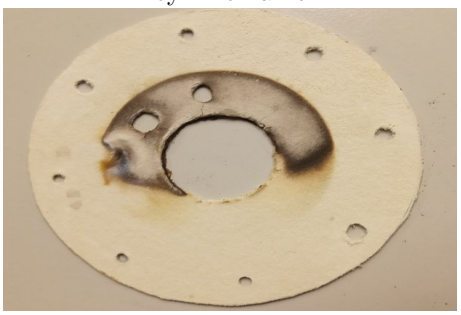

(c) Isoplan 1000 (insulating material) burnt by zinc flame (surface area exposed to the shroud flow region)

(d) Isoplan 1000(insulating material) burnt by zinc flame (surface area in contact to the aluminium top plate)

Figure 6.1: Effect of zinc flame propogation towards the aerosol exit

As the maximum flame temperature of zinc is around 1587°C [51], the propagation of flame towards the exit of the aerosol jet damaged the heating system in the top plate. The aerogel and the isoplan which were used as insulating material to prevent heat loss in the top plate were burnt due to its limited temperature resistance as seen in figure 6.1(c) and (d). The heat popagated in the shroud flow region inside the top plate with pure oxygen flow. This increased the temperature inside the top plate much higher than the zinc flame temperature, resulting in damage of mica heating element as seen in figure 6.1(a). As the zinc oxide is a vapor phase combustion product, the zinc oxide deposits on the heating elements and covers the zinc aerosol exit (of 1 mm diameter). This vaporised zinc oxide also damaged the gas lighter. The flame flashback could be due to the reduced velocity of zinc particles in the jet. Moreover, the flame does not occur at all successive

tests due to the decrease of zinc aerosol concentration in the flow. From figure 6.1(b), yellow deposits of zinc oxides are observed, which is caused by the thermochromic property of zinc oxide. Due to the high temperature inside the preheating chamber (top electrode), zinc oxides change from white to yellow. This color change is caused by a small loss of oxygen to the environment at high temperatures to form the non-stoichiometric $Zn_{1+x}O$. Furthermore, the aerogel thickness was decreased and solidified (loss of aerogel) due to its limited temperature resistance (650°C). Even though Isoplan 1000 can withstand 800°C degrees, smoldering occurs on its surface because of high flame temperature of zinc flame, which is shown in figure 6.1(c). Zn-1 powder with preheated pure oxygen flow, did not combust in absence of gas lighter.

Replacing the mica heating element and the insulating material (aerogel and isoplan-1000), the experiments were conducted for detailed observation of combustability with Zn-2 powder to determine the combustability of zinc with pure oxygen in both flow. In the burner setup with preheater, the study was carried out with heating element turned off. The velocity of the central jet and shroud flow remain 100 cm/s and 6 cm/s with 100 % oxygen concentration in both flow. The aerosol jet was stable, the jet cloud burns with the gas lighter but zinc cloud ignition (flame) does not occur. Thus, heating element was set to 300°C using the temperature controller. A quartz tube was placed on the exit of the aerosol jet to prevent the heat loss and to maintain less temperature difference throughout the aerosol. The aerosol jet ignited (burned brightly) but burned-out immediately in absence of gas lighter. The temperature was further increased to 500°C with same flow rate and oxygen concentration. The flame ignition was predominately seen and flame wass not achieved. So, the velocity of the central jet was increased to 140 cm/s and shroud flow remained 6 cm/s with 100 % oxygen concentration in both flow. The temperature of the heating element was also increased to 600°C, the aerosol had flame and it started propagating towards the aerosol exit. The insulating material (aerogel and the isoplan-1000) gets burnt due to high flame temperature but the damage is as little as compared to previous test. The smouldering of aerogel is observed for few minutes. From figure 3.14, the temperature of the flow at the around 400°C (heating elements temperature is 700°C) with pure oxygen concentration, the zinc combustion occurs with a flame but burn-out happens due to the flash-back of the flame. The number density and velocity of zinc particles in the flow would be the reason for the flash-back.

6.1.2 Flammability test using burner without preheating

Flame propogation is not observed in all trials and in most experiments, the jet burned only in the presence of a gas lighter. One of the reason might be the zinc concentration in the flow as the central jet at the exit of the top plate has an area of 0.785 mm^2. So, the amount of zinc particles in the flow needed to be increased. This was achieved by increase in central jet area (by enlarging the diameter of the hole in the top plate). The top plate with preheater is needed for other experiments, its central flow area was decided not to increase. Thus the combustability of zinc at higher particle concentration were carried out in burner without preheating. In that case, the top plate (stainless steel which is the top electrode without preheating system) hole diameter was increased from 1 mm to 2 mm. Due to increased flow area (3.14 mm^2), the gas flow rate needs to be increased inorder to achieve the same volumetric flow rate of the aerosol. As the flow rate of MFC with pure oxygen in the central jet is limited to 50 mL/min, the maximum velocity of oxygen flow achieved is 120 cm/s. This limitation was increased by interchanging the gas connections of oxygen and nitrogen flow in the MFC on the gas supply board. Table 6.2 shows the maximum gas flow rate of MFC's and its details used for increased central jet flow area (3.14 mm^2). This resulted in achieving a maximum flow speed (363 cm/s) of pure oxygen in the central jet. The gas flow and operational features of MFC can be found in Appendix .1.

The velocity of the central jet and shroud flow was set to 200 cm/s and 6 cm/s with 100 % oxygen concentration in both flow. The zinc aerosol ignited with a bright flame but it blew off immediately. Several trails were carried out by increasing and decreasing the velocity of the central

Table 6.2: MFC details used for increased central jet flow area (3.14mm^2)

Central jet area 3.14 mm2				
	Central jet		**Shroud flow**	
MFC	1	2	3	4
MFC Number	MFC-30	MFC-40	MFC-33	MFC-9
Gas Used	Oxygen	Oxygen	Oxygen	Nitrogen
MOB Port No	4	3	2	1
Max Flow Rate [Ln/min]	0.2	0.049	5.263	5.136

jet. Around 170 cm/s of central jet speed, the zinc aerosol ignited and a flame for 4 to 5 seconds was achieved. During many trials, the flame started to propogate downwards and blows off at the exit of central jet in the top plate as can be seen in figure 6.2 (c). Figure 6.2 (a) and (b) show a zinc combustion with white and bluish flame. The concentration of oxygen was also increased and decreased to check the flammability of zinc aerosol (higher concentration of zinc particles in 3.14 mm^2). Zinc aerosol had flame followed by a flash-back when the oxygen concentration was around 75 % to 100 %. Thus, increase in top plate diameter resulted in a flame for few seconds. Moreover, the zinc ignition occured with 75 % oxygen concentration without preheating the aerosol, whereas in preheating system 100 % oxygen concentration was needed for its ignition. If the diameter of the preheating top plate is also increased, it is possible to achieve a stable flame in low oxygen concentration with preheated zinc aerosol. Zn-1 powder did not combust in this increased central jet area burner setup. As inferred from the experiments, the Zn-2 powder is more coarse and high purity than Zn-1. The diameter of the Zn-2 powder was not determined during the analysis due to time constraints. It could be interesting to analyze its average diameter using optical microscope. Since the zinc melting point is less than its flame temperature, during flame the burn-out and flash-back occurred often. Increase in particle size could have a considerable effect in having a stable flame without flash-back. Different diameter of top plate hole between 1 to 2 *mm* could also be investigated with and without preheating system, which gives better insights about flame stabilization and propagation of zinc aerosol. The zinc oxide formed during the experiments observed to be much smaller in size. If they were captured and invesitigated in SEM gives an overview of size and structure of the zinc oxide formed.

The activation energy required for the oxidation of zinc is an interesting aspect to study for a stable combustion. The amount of zinc and oxygen over a time period in the flow is not sufficient for a stable flame. Moreover, preheating the aerosols increase the rate of the reaction. This preheating has a direct relation to the heat released during the combustion reaction. The amount of heat released during preheating has lower activation energy as compared to the non-preheated mixture. Detailed study of reactants activation energy and heat release would help in better understanding the zinc aerosol ignition and flame stabilization (preventing the flashback and burnout of zinc aerosol flame).

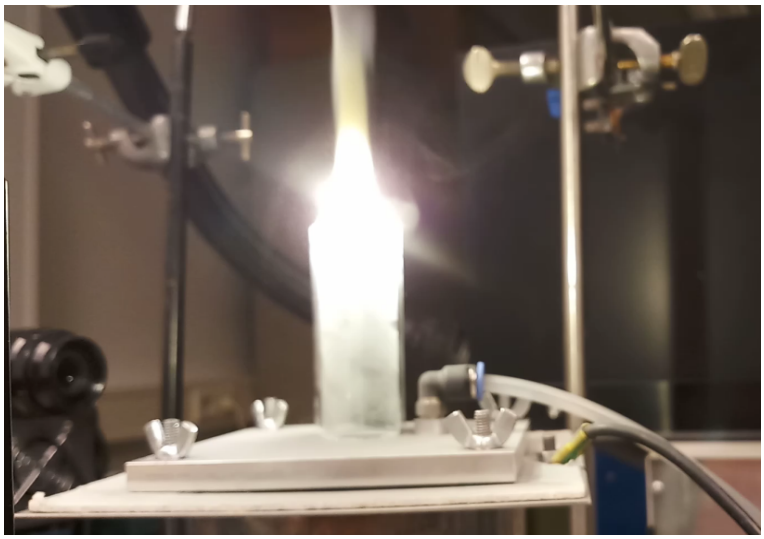

(a) Zinc combustion with white flame

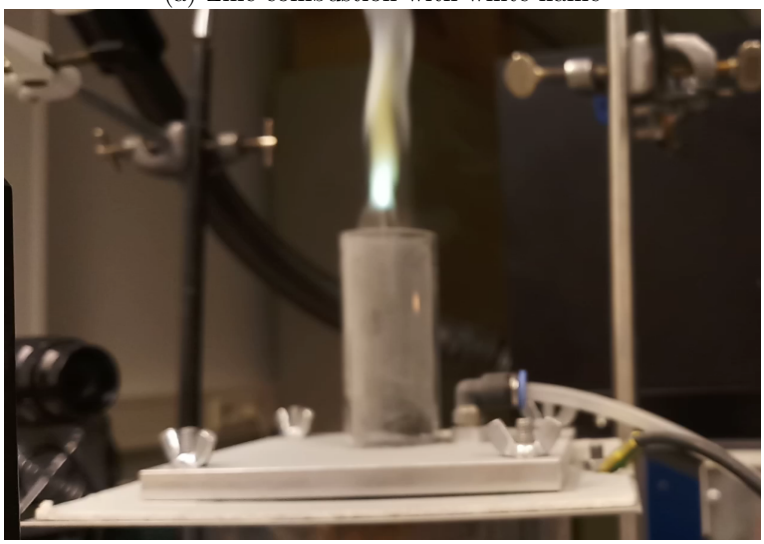

(b) Zinc combustion with bluish flame

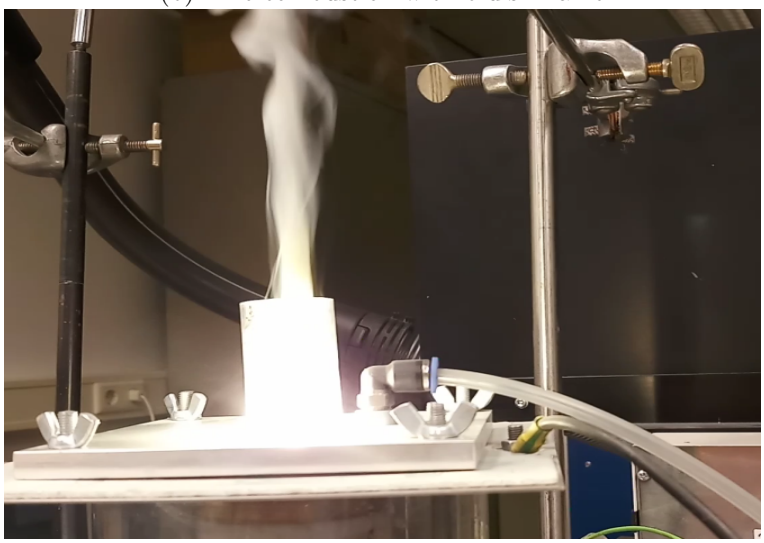

(c)Flame propogation towards the central jet exit from the top plate

Figure 6.2: Burner without preheating system of central jet area of top plate with 3.14mm^2

Chapter 7

Conclusions

Metals and specifically metal powders are a promising group of energy carriers with zero-carbon recyclable fuel option. They have high energy density, high power density, excellent recyclability and some of these are abundant on Earth. This makes metals a promising sustainable energy source in the future. Iron is one of the most abundant metals present on Earth, composing 35% of Earth's mass. It is estimated that there are 800 billion tons of iron ore resources found worlwide, in which 230 billion tons mainly in countries such as Australia, Russia, Brazil, India and USA. Likewise, zinc is an ubiquitous metal occurring in many rocks on Earths crust, with an availability of 14 million metric tonnes produced worldwide. Research of metal aerosol combustion in past few decades helps in exploring the combustion behavior of metal powders of different sizes and concentrations. In order to understand the characteristics much better, an efficient metal particle suspension burner is needed. One such burner is developed at Eindhoven University of Technology by the Metal Fuel research group. However, characteristics of the aerosol during dispersion by the burner are unknown. Moreover, combustability of zinc in such burner system was also not determined. To get insights about the iron aerosol characteristics (such as particle velocity and number density) and zinc aerosol combustability, various experiments were carried out.

In chapter 2, the background of the aerosol combustion of iron and zinc metal were discussed in reference to literatures. The working of Micro Metal Dust Burner (M^2DB) and its parts were explained. Following that in Chapter 3, new lower electrode was designed with increased brim radius to prevent particle loss around the lower electrode during dispersion. This prevented the particle settling inside the chamber. The electric potential around the brim decreased due to its increased edge radius. The top electrode with preheating is assembled with heat insulators in order to prevent maximum heat transfer (forced convection heats the airflow inside the top electrode) and the aerosol jet was stabilized by increasing the shroud flow area inside the top electrode.

Two preheaters were tested during the experiments, in which mica heating element provided better results in terms of preheating the shroud flow when compared to inline preheater. PID controller used for mica heating element had higher temperature fluctuations when the transformer in the controller was increased to higher values (50 and 100 W). Increase in power supply of the controller results in higher gain which makes the process variable (feedback from the controller) to oscillate resulting in large temperature fluctuations. Temperature measured at two positions at the exit of the top plate has temperature difference from 40°C to 100°C when the temperature of the heating element was increased to a power supply of 35 W. Temperature profile for increased power of 50 W was recorded for different set points in the tempearture controller. Temperature based on height of the jet was also measured for different temperature setpoints. Variable voltage controller had stable temperature profile measured at the centre of the aerosol exit. The increased heat loss at higher temperature could be prevented by adding a tubular heater (nichrome wire winded on the quartz tube) on the top aerosol exit. The optimized PID control in terms of reduced fluctuation at higher power results in efficient heating of the air flow.

Velocity of the iron particles in the air flow was determined by performing optical diagnostics on the aerosol jet. Images were taken based on the preferred region of interest in the flow, and post process was done in PIV View interface using autocorrelation function. Particle velocity was determined from the particle displacement data. The velocity contour of the iron particles in the flow had a maximum velocity of 0.32 m/s and a minimum velocity of 0.1 m/s. Increased density of the iron particles due to the settling effect caused by gravitational force; a cloud of iron particles form a stable zone where the flame occurs. Since the displacement of the particles were low around this region, post processing the images taken with a neutral density filter did not result in a clear velocity field.

Number density estimation of iron aerosol was carried out by capturing the metal oxides using a membrane filter. Settling velocity of the particles calculated was 0.035 m/s and the average number density of the iron particles in the flow was estimated as $7.36 \cdot 10^5$ 1/cm^3. Captured metal particles resulted in presence of two types of oxides: magnetite (grey in color) and hematite (yellow and reddish brown in color). Increased oxygen concentration lead to prominant occurence of hematite. The diameter of the oxides were analyzed in optical and scanning electron mircoscopes by collecting the samples in a glass plate. The sample collected near the iron flame, combusted in normal air had particles with size around 6 μm, whereas the sample at height of 10 cm had oxides of size larger than 15 μm. Iron oxides collected from normal air were micron sized oxides but the iron oxides formed from 60% oxygen concentration were mostly nano sized oxides. SEM analysis performed on the samples collected in the glass plate resulted in unclear images and the structure of the oxide formed were hard to determine. However, the presence of nano-oxides at 60% oxygen concentration and micron-sized oxides at 21% oxygen concentration were visualized. Sample of oxides collected in conductive metal like copper would result in analyzing the structure of oxides formed. Iron undergo heterogeneous combustion forming gaseous oxides and sub-oxides which were in nanometers formed in higher oxygen concentration. On other hand, forming porous oxide shell of micrometers in size where the oxygen reacts with the outer shell of iron and this reaction happens in normal air. This could be interesting to analyze.

Finally, the zinc aerosol combustability was investigated. Zinc aerosol(209988 Aldrich) of size less than 10 μm does not yield any result. Zinc (96454 Aldrich) of unknown diameter was used in the experiments. With the preheating system, at 600°C in the heating element, the zinc aerosol ignited resulting in an unstable flame, with flash-back. This propagation would be due to the aerosol density. Increased flow area of zinc aerosol without preheating was tested for a stable flame. Zinc aerosol had a stable flame for 4 seconds and then the flame propagation happened prominently. Ignition of zinc cloud occured when the oxygen concentration was around 75%, but still flash-back occurs. This might be due to the low flow rate of the jet for that flow area and particle size. Increased particle size would have better effect on flash-back and also flow area between 0.785 mm^2 and 3.14 mm^2 has to be tested. Flow rate has to be varied accordingly based on the flow area. Moreover, a simple quartz tube with nichrome wire insulated could be used as a tube heater above the top plate which helps in uniform temperature for the jet. Temperature around 600°C near the flame zone, would result in combustion of zinc aerosol to burn in air. The size of the zinc oxide appeared to be lesser in size than iron oxides preferably around 1 μm. It would be interesting to find the structure and diameter of the zinc oxide if a stable flame is achieved. Due to time constraint the proposed investigation was not carried out.

Bibliography

[1] J. H. Sun, R. Dobashi, and T.Hirano, "Combustion behavior of iron particles suspended in air," *Combustion Science and Technology*, vol. 150, pp. 99–114, 2000. ix, 6, 7

[2] M. V. Stiphout, ""Design and Development of a Micro Metal Fuel Burner"," *Master Thesis*, 2017. ix, ix, 2, 12, 13

[3] A. Gore, "The End Of Fossil Fuels," 2017. 1

[4] "CO_2 emissions," 2017. 1

[5] M. A. Maehlum, "Fossil Fuels Pros and Cons Fuels," May 2013. 1

[6] B. Koerner, "The Other Greenhouse Gases," November 2007. 1

[7] J. Bergthorson, " Metal particles, the clean fuel of the future," December 2015. 2

[8] M. K. King, "Ignition and combustion of boron particles and clouds," *Journal of Spacecraft and Rockets*, vol. 19, no. 4, pp. 294–306, 1982. 2

[9] C. L. Yeh, and K. K. Kuo, "ignition and combustion of boron particles," *Progress in Energy and Combustion Science*, vol. 22, no. 6, pp. 511–541, 1996. 2

[10] D. Liu, Z. Xia, L. Huang, and J. Hu, "Boron Particle Combustion in Solid Rocket Ramjets," *Journal of Aerospace Engineering*, vol. 28, no. 4, October 2014. 2

[11] M. Beckstead, "A summary of aluminum combustion, in Internal Aerodynamics in Solid Rocket Propulsion," *RTO/ NATO*, vol. 23, no. 5, pp. 1–17, January 2014. 2

[12] M. Hertzberg, I. A. Zlochower, and K. L. Cashdollar, "Metal dust combustion: Explosion limits, pressures, and temperatures," 2, 6

[13] H. Y. Lin, Y. W. Chen, and C. Li, "The mechanism of reduction of iron oxide by hydrogen," *Thermochimica Acta*, vol. 400, pp. 61–67, 2003. 2

[14] J. Bergthorson, S. Goroshin, M. Soo, P. Julien, J. Palecka, D. Frost, and D. Jarvis, "Direct combustion of recyclable metal fuels for zero-carbon heat and power," *Applied Energy*, vol. 160, pp. 368–382, 2015. 2

[15] K. Kleiner, "The iron age," *New Scientist*, vol. 188, pp. 35–37, 2005. 2

[16] D. Beach, A. Rondinone, B. Sumpter, S. Labinov, and R. Richards, "Solid-state combustion of metallic nanoparticles: New possibilities for an alternative energy carrier," *Journal of Energy Resources Technology*, vol. 129, pp. 29–32, 2007. 2

[17] V. Utgikar, W. Lattin, and R. Jacobsen, "Nanometallic fuels for transportation: A well-to-wheels analysis," *International Journal of Energy Research*, vol. 31, pp. 99–108, 2007. 2

[18] N. Auner and S. Holl, "Silicon as energy carrier-facts and perspectives," *Energy*, vol. 31, pp. 1395–1402, 2006. 2

[19] D. Wenl, "Nanofuel as a potential secondary energy carrier," *Energy and Environmental Science*, vol. 3, pp. 591–600, 2010. 2

[20] S. Goroshin, F.-D. Tang, A. J. Higgins, and J. H. Lee, "Laminar dust flames in a reduced-gravity environment," *Acta Astronautica*, vol. 68, pp. 656–666, 2011. 2

[21] " HISTORY OF THE AEROSOL." 5

[22] H. M. Cassel, "Some fundamental aspects of dust flames," *Bureau of Mines*. 5

[23] D. R. Ballal, "Further studies on the ignition and flame quenching of quiescent dust clouds," *Proceedings of the Royal Society of London A*, vol. 385, pp. 1–19, 1983. 5

[24] D. R. Ballal, "Flame propagation through dust clouds of carbon, coal aluminium and magnesium in an environment of zero gravity," *Proceedings of the Royal Society of London A*, vol. 385, pp. 21–51, 1983. 5

[25] M. Hertzberg, I. A. Zlochower, and K. L. Cashdollar, "Metal dust combustion: Explosion limits, pressures, and temperatures," *Symposium (International) on Combustion*, vol. 24, no. 1, pp. 1827–1835, 1992. 6

[26] T. Skjold, and R. Eckhoff, "Dust Explosions in the Process Industries:Research in the Twenty-first Century," *Chemical Engineering Transactions*, vol. 48, pp. 337–342, 2016. 6

[27] J. H. Sun, R. Dobashi, and T. Hirano, "Structure of flames propagating through metal particle clouds and behavior of particles," *Symposium (International) on Combustion*, vol. 27, pp. 2405–2411, 1998. 6

[28] T. Hirano, Y. Sato, and J. Sato, "The Rate Determining Process of Iron Oxidation at Combustion in High Pressure Oxygen," *Oxidation Communications*, vol. 6, no. 1-4, pp. 113–124, 1984. 6

[29] T. Hirano, and J. Sato, "Fire Spread along Structural Metal Pieces in Oxygen," *Loss Prevention in Process Industries*, vol. 6(3), pp. 151–157, 1993. 6

[30] T. Hirano, Y. Sato, and J. Sato, "Fire Spread Mechanisms along Steel Cylinders in High Pressure Oxygen," *Combustion and Flame*, vol. 51, pp. 279–287, 1983. 6

[31] E. A. Jenkins and E. W. Harvey, *Fundamentals of Optics, Fourth Edition*. McGraw-Hill Book Company, 1976. 7

[32] J-H. Sun, R. Dobashi, and T.Hirano, "Temperature profile across the combustion zone propagating through an iron particle cloud," *Journal of Loss Prevention in the Process Industries*, vol. 14(6), pp. 463–467, 2001. 8

[33] J-H. Sun, R. Dobashi, and T. Hirano, "Concentration profile of particles across a flame propagating through an iron particle cloud," *Combustion and Flame*, vol. 134(4), pp. 381–387, 2003. 8

[34] J-H. Sun, R. Dobashi, and T. Hirano, "Velocity and number density profiles of particles across upward and downward flame propagating through iron particle clouds," *Journal of Loss Prevention in the Process Industries*, vol. 19(2-3), pp. 135–141, 2006. 8

[35] F-D. Tang, S. Goroshin, A. Higgins, and J. Lee, "Flame propagation and quenching in iron dust clouds," *Proceedings of the Combustion Institute*, vol. 32, pp. 1905–1912, 2009. 8

[36] F-D. Tang, S. Goroshin, and A. Higgins, "Modes of particle combustion in iron dust flames," *Proceedings of the Combustion Institute*, vol. 33, pp. 1975–1982, 2011. 8

[37] N. Poletaev, A. Zolotko, and Y. Doroshenko, "Degree of dispersion of metal combustion products in a laminar dust flame," *Combustion, Explosion, and Shock Waves*, vol. 47(2), pp. 153–165, 2011. 8

[38] A. Wright, "Investigation of discrete flame propagation regime in particulate suspension," *McGill University (Masters thesis),*, 2015. 8

[39] A. Haghiri and M. Bidabadi, "Dynamic behavior of particles across flame propagation through micro-iron dust cloud with thermal radiation effect," *Elsevier Fuel*, vol. 90, pp. 2413–2421, 2011. 8

[40] M. Broumand and M. Bidabadi, "Modeling combustion of micron-sized iron dust particles during flame propagation in a vertical duct," *Fire Safety Journal*, vol. 59, pp. 89–93, 2013. 8

[41] M. Bidabadi, M. Hajilou, A. K. Poorfar, S. H. Yosefi, and S. Zadsirjan, "Modeling flame propagation of micron-sized iron dust particles in media with spatially discrete sources," *Fire Safety Journal*, vol. 69, pp. 111–116, 2014. 8

[42] P. Julien, S. Whiteley, S. Goroshin, M. J. Soo, D. L. Frost, and J. M. Bergthorson, "Flame structure and particle-combustion regimes in premixed methane-iron-air suspensions," *Proceedings of the Combustion Institute*, vol. 35, pp. 2431–2438, 2015. 8

[43] A. Moezzi, A. M. McDonagh, and M. B. Cortie, "Zinc oxide particles: synthesis, properties and applications," *J. Chem. Eng*, vol. 185-186, pp. 1–22, 2012. 9

[44] M. E. Derevyaga, L. N. Stesik, and E. A. Fedorin, "Ignition and combustion of aluminium and zinc in air," *Fizika goreniya i vzryva*, vol. 13, no. 6, pp. 852–857, 1976. 9

[45] S. Rackauskas, S. D. Shandakov, O. Klimova, H.Jiang, E. I. Kauppinen, A. Nikitenko, O. V. Tolochko, K. A. Chernenko, and A. G. Nasibulin , "A novel method for continuous synthesis of Zno tetrapods," *The journal of physical chemistry*, vol. 119, pp. 16366–16373, June 2015. 9

[46] N. I. Poletaev, M. Y. Khlebnikova, and K. Y. Khanchych, "Producing and properties of zinc dust ames," *Taylor and Francis Group*, january 2018. 9

[47] C. sen Wang, *Inhaled Particles.* Interface Science and Technology, 2005. 10, 11

[48] M. D. Hays, "Analysis of the chemical and physical properties of combustion aerosols:," January, 2013. 10

[49] C. N. Davies, "Definitive equation for the fluid resistance of spheres," *Proceedings of Physics Society*, vol. 57, pp. 259–270, 1945. 11

[50] J. C.-J. Tien, *Practical Mine ventilation Engineering.* Intertec Micromedia Publishing Company, March 1999. 31

[51] ""Metals and alloys"," *Factory Mutual Insurance Company (FM Global)*, pp. 7–85, July 2015. 43, 44

Appendix A

Laboratory Setup and Technical Specifications

The burner setup has central jet and shroud flow which suspend the metal particle to form a stable jet. The gas for the apparatus is supplied from the gas supply board as shown in the figure 1. The gas used in the experiment are oxygen and nitrogen. All connections and fixed elements are connected by mini industrial couplers. The gas through the tubings are connected with RECTUS 21-series coupling elements and then to DN-5 sized quick connectors with a flow area of 314 mm^2. Then, using push-in fittings and connectors with polymer tubing, the gas flow is supplied to the apparatus. The flow rate and the oxygen concentration are controlled by Bronkhorst mass flow controllers. Mass flow controllers are analogously controlled using NI-DAQmx control system with the help of LabVIEW interface. From table 3.1, the gas used and the maximum flow rate using the mass flow controllers along with their MFC number. The MFC number is also labelled in the figure 1 for better understanding the gas supply board.

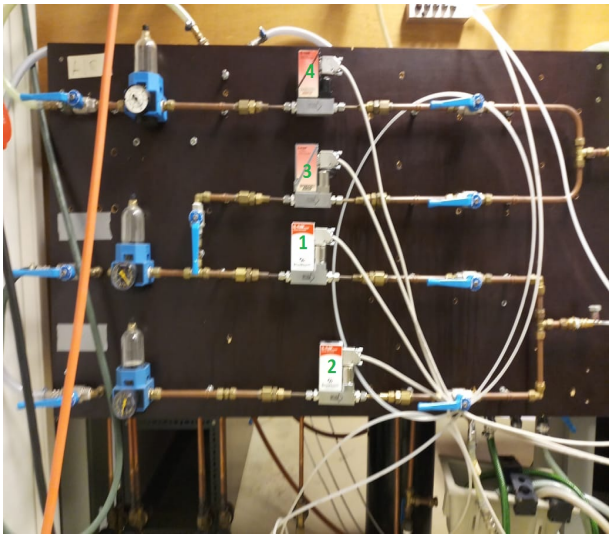

Figure A.1: Gas supply board

It is chosen to control the MFCs in analogue mode, using existing NI-DAQmx control units, combined with a LabVIEW user interface. In principle always a mixture of oxygen and an inert gas (most commonly nitrogen) is used for both the particle laden flow and the shroud flow. Both mixtures could be controlled independently and allow oxygen concentration ranging from 0%

to 100%. The final control program is based on a in-house developed LabVIEW program for controlling premixed combustible gas/air mixtures as shown in the figure 2. The distance between the lower capacitor and upper electrode is 4mm (which can be decreased by removing the spacor rings), the maximum voltage could be applied is 9 kV after that the electric spark occurs inside the chamber. When the distance between the electrodes is increased, the number density would change in the flow. Since iron burns at low concentration in the flow and for optical analysis, few particles in the flow is needed, so the distance between the electrodes is reduced. In that case single particle analysis could also be done. Based on the metal dust concentration the aerosol jet forms a stable flame front where the flame zone occurs. By changing the flow speed of central jet in the LabVIEW software, the jet height can be increased or decreased. The applied voltage controls the density of the particles in the flow. There are two capacitors used, one with larger depth to hold metal dust and another with larger width. The capacitor with larger depth and increased brim geometry which reduces the particle loss very effectively, particularly at reduced distance between the electrodes. Technical drawings for the lower electrode with larger depth can be seen in the figure 3. The redesigned top aluminium casing for increased shroud flow area inside the top plate is shown in the figure 4.

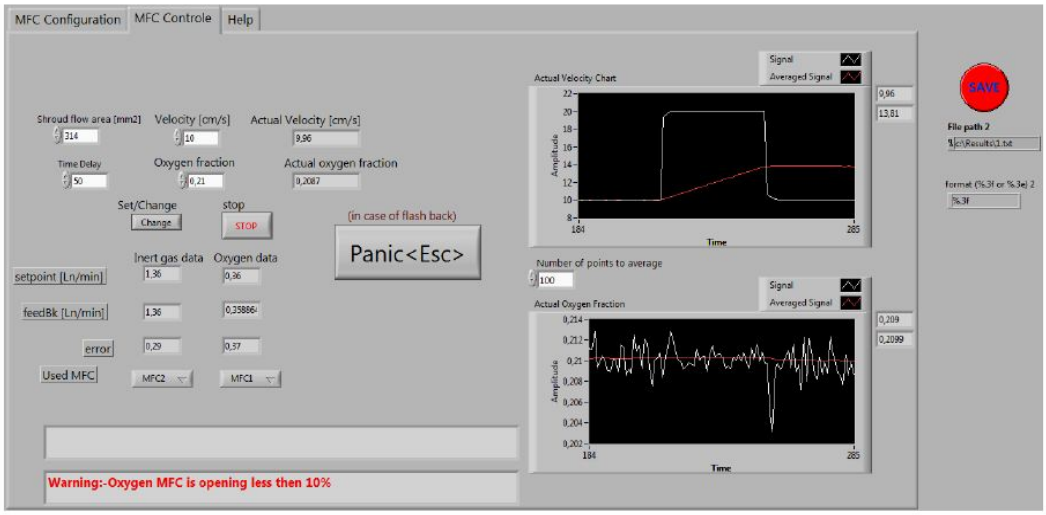

Figure A.2: Labview interface for shroud flow control. A change in setpoint of 10 to 20 cm/s and back to 10 cm/s is shown

A.1 Heating element

Two heating system are used in the experiments to analyse the effect of preheating in the burner setup. The inline preheater (Omega AHP-7562) is used to preheat the shroud flow which has a maximum power of 750W and maximum temperature it can reach is 813K. Since, the minimum flow rate required by the heater is larger than the usual gas flow rate used, strategy to efficiently use the heater has to be defined. Currently, the inline preheater is not connected to the burner system as the heating coil inside is damaged. It can be replaced or a new heater has to ordered based on the flow rate used. The PID controller to control the inline preheater has a power supply voltage of 240V and 750W. A thermouple inside the inline preheater is connected to the PID controller which gets feedback to adjust the temperature of the heater based on temperature setpoints. The flat mica heating element (Calesco M104718) with maximum 24 V and 190W is assembled inside the top plate elevtrode. A thermocouple placed between the mica heater and aerogel insulation material is connected to the PID controller which works in a similiar way like the other PID controller. This PID controller has an output power of 50W which has the maximum

temperature reach of 685 $°C$, which can be increased or decreased by changing the transformer of the controller.

A.1.1 Optical Analysis

The DIY laser poduces the continuous laser beam which can be modulated using a DG1000 Arbitrary waveform function generator. As the laser has high power of 5W reducing the intensity of the laser beam by reducing the duty cycle to 5% is necessary. The laser beam is focused using a covex and concave lens placed between the laser beam and the burner. A thin laser sheet is created by focussing the laser beam and adjusting the lens inbetween. The camera system is placed perpendicular to the laser sheet created. The burner is mounted on a supporting jack which has three axis of adjustment during optical analysis. Thus, enabling it to adjust the movement of the burner based on laser sheet, camera and region of interest in the aerosol flow. The camera (TM 2040-GE) is connected to a stanford DG535 trigger box which controls the exposure time and record the captured images. The JAI SDK program is used to change the pixel length and width of the CCD camera used. Based on the focal length needed, the lens can be used from the laser lab optical section. The pulsewidth control operation mode is used during the experiments. There are several modes available based on the analaysis in the JAI-SDK software. In the trigger box, the external frequency used is 10Hz. The trigger output signal types used are given in the following table 1. The A intergal B function is used with A = T + 6 μs and B =68 ms. The post processing of images are done in PIV view with autocorrelation mode.

Table A.1: Trigger output signal types used for PIV analysis

Trigger output signal		
To	Load 50	TTL:Normal
A	Load 50	TTL:Normal
B	Load 50	TTL:Normal
C	Load 50	TTL:Normal
D	Load HighZ	TTL:Normal

A.2 Cooling Channel in Top electrode

Since the top electrode can reach upto temperature of 600$°C$, water circulation inside the top plate prevents the heat transfer to the dispersion chamber. The flow rate can be regulated using a flow meter which has a maximum flow rate of 100mL/min. For preventing the flow rate downwards, flow rate of 10mL/min is suffice for the top plate. The outflow water is directed to a temporary storage water container, which should be emptied after every experiments if possible, to prevent the overflow.

A.3 Safety instructions

The gas supply board regulates the flow of oxygen and nitrogen to the burner system. When the burner setup is not used, the gas supply valve has to be closed to prevent the flow of oxygen and nitrogen eventhough it is not dangerous, since normal air concentration is used. When experiments are conducted, the ventilation has to be turned onto capture the metal oxide fumes. Furthermore, the optical setup has to be covered to prevent the dust exposure on lens. The HEPA filter vacuum cleaner can be used to capture the particles which remains on the top plate and table. Safety glasses for laser could be used if needed during experiments. Top plate has to be grounded whenever it

is remounted after loading the metal particles in the lower electrode. The water supply for the cooling channels during preheating is closed after the experiment is carried out to prevent the water flow inside the laser lab.

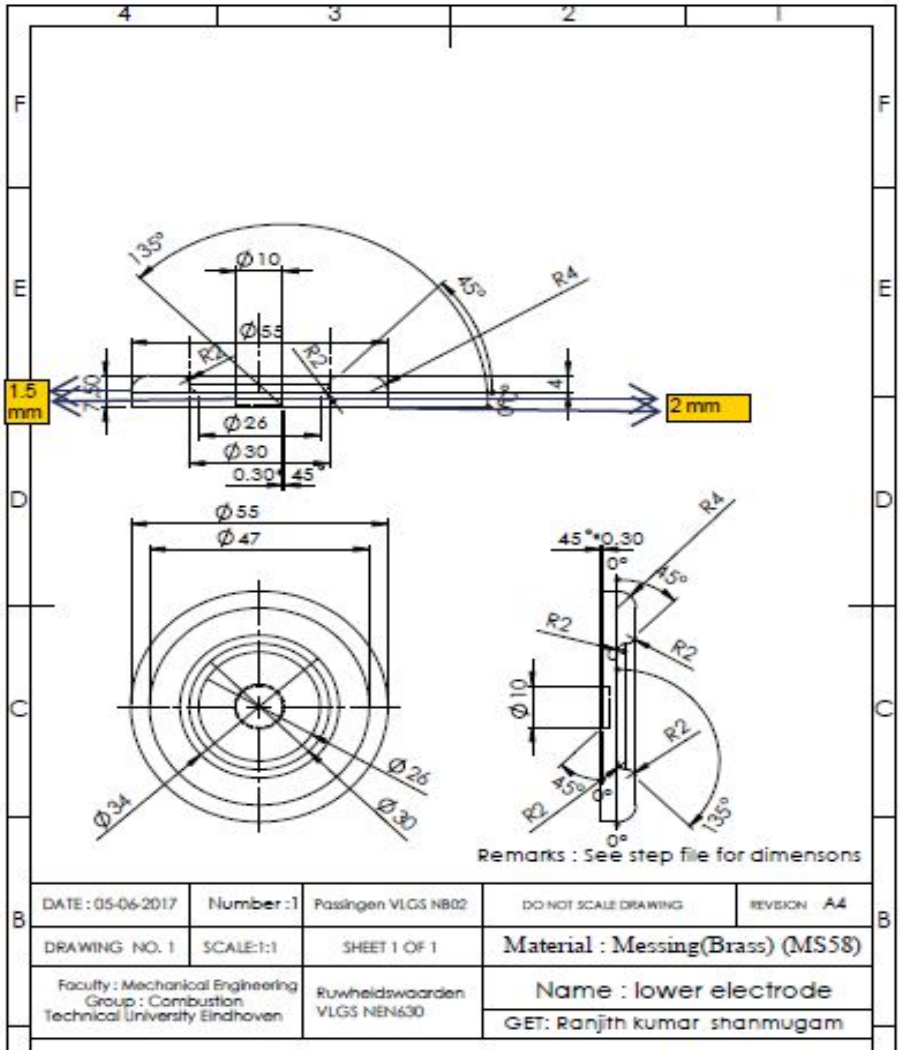

Figure A.3: Technical drawing for the new capacitor (lower electrode)

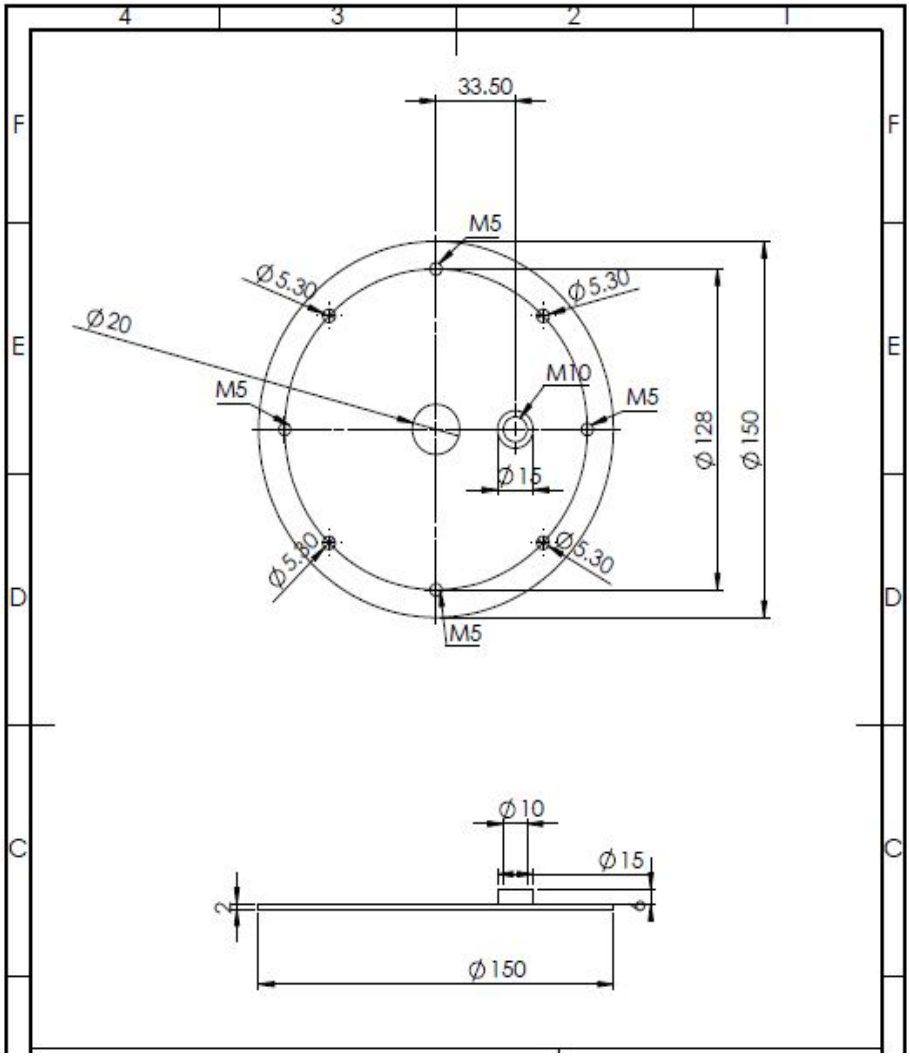

Figure A.4: Technical drawing for the top alunium casing for top plate

Appendix B

Preheating

The final upper electrode is optimized in a number of subsequent steps as described in the section . Two types of insulation material used in the system are aerogel blankets and Frenzelit isoplan 1000 GREENLINE. Aerogel standard blanket of 3 mm thickness which has a thermal conductivity of 0.018 $W/(mK)$. Isoplan 1000 of 2 mm thickness is used inside and outside of the top plate. It is a combination of bio-soluble mineral fibre and temperature-resistant filling agents. It has thermal conductivities ranging from 0.11 $W/(mK)$ at ambient conditions to 0.14 $W/(mK)$ at $850K$. The position of the thermocouple at two radius during temperature measurements at top plate gas flow exit is shown in the figure 5.

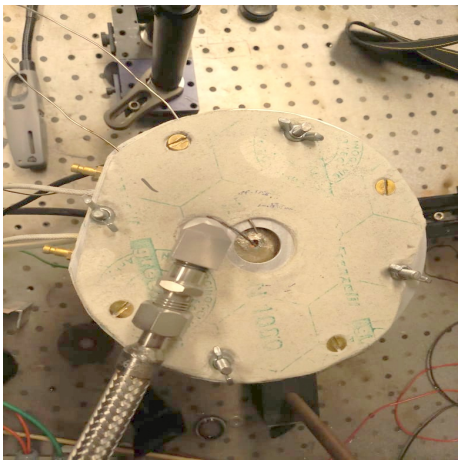

Figure B.1: Position of the thermocouples at Top plate gas exit for Temperature measurement of the preheated gas flow gas

After the temperature of the gas flow measured at different radius, the temperature profile based on height was determined. The thermocouple is positioned at different height from the heating element and the tempearture difference is evaluated. Heater temperature above $550°C$ is plotted and detailed in section . The temperature distribution of gas flow below $550°C$ if the heating element is shown in the following figures 6 7 8 9. Since the controller has greater temperature fluctuation in the measurements below $550°C$, the temperature measured are also differs by $50°C$. Moreover, the heat dissipation of the preheated gas flow to the external surface, the difference of temperature at 1 cm and other height varies $80°C$. This difference can be compensated by adding a tubular heater to the top plate or insulating the quartz tube to prevent the heat loss. Either way affects the optical access to the jet inside the tube. The idea of winding nichrome over quartz tube could be experimented. This might provide good results enabling visual

access to the flow.

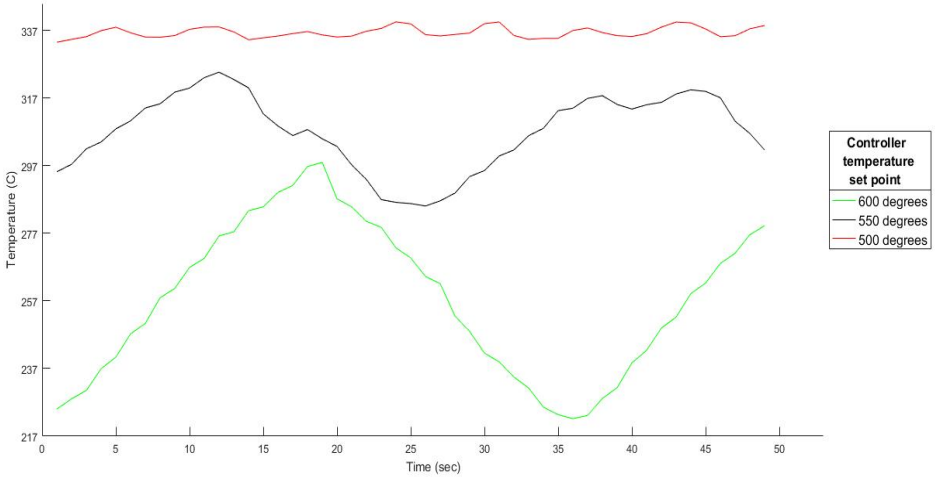

Figure B.2: Temperature of the preheated gas flow gas (central jet and shroud flow) at a height of 1 cm)(Thermocouple at the centre of the topplate)

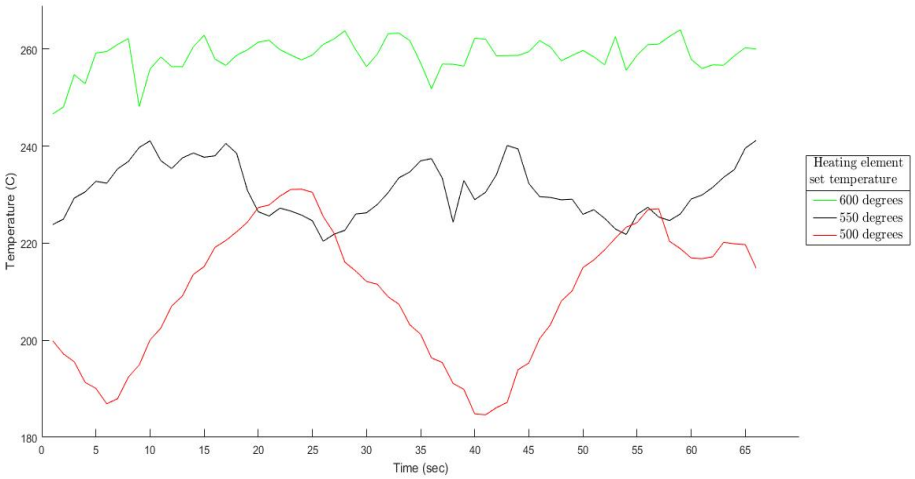

Figure B.3: Temperature of the preheated gas flow gas (central jet and shroud flow) at a height of 2 cm)(Thermocouple at the centre of the topplate)

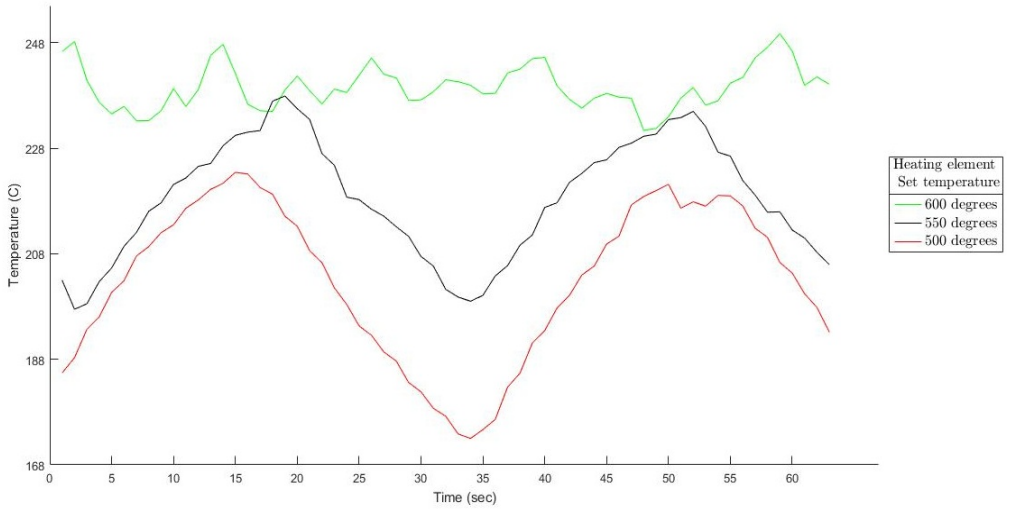

Figure B.4: Temperature of the preheated gas flow gas (central jet and shroud flow) at a height of 3 cm)(Thermocouple at the centre of the topplate)

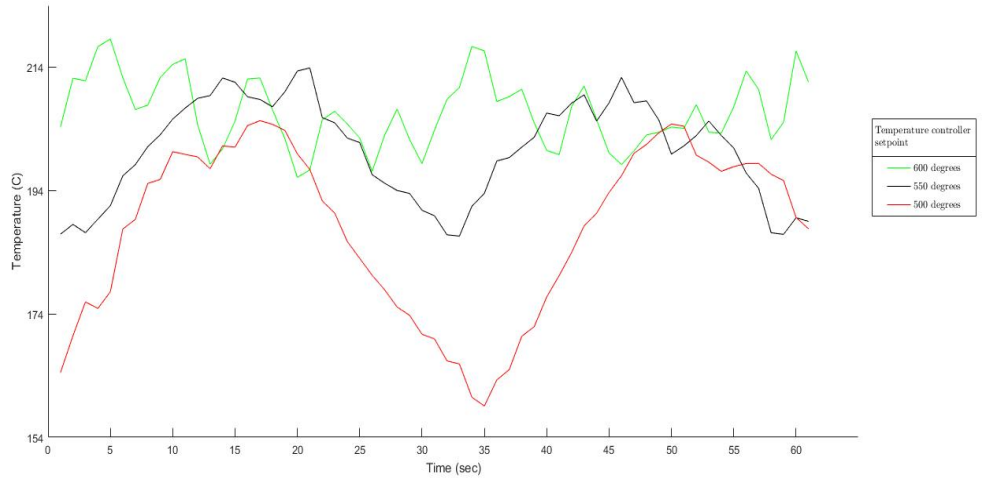

Figure B.5: Temperature of the preheated gas flow gas (central jet and shroud flow) at a height of 4 cm)(Thermocouple at the centre of the topplate)